

Photoproduction of pions and properties of baryon resonances from a Bonn-Gatchina partial wave analysis

A.V. Anisovich^{1,2}, E. Klempt¹, V.A. Nikonov^{1,2}, M.A. Matveev^{1,2}, A.V. Sarantsev^{1,2}, U. Thoma¹

¹ Helmholtz-Institut für Strahlen- und Kernphysik, Universität Bonn, Germany

² Petersburg Nuclear Physics Institute, Gatchina, Russia

Received: October 15, 2018/ Revised version:

Abstract. Masses, widths and photocouplings of baryon resonances are determined in a coupled-channel partial wave analysis of a large variety of data. The Bonn-Gatchina partial wave formalism is extended to include a decomposition of t- and u-exchange amplitudes into individual partial waves. The multipole transition amplitudes for $\gamma p \rightarrow p\pi^0$ and $\gamma p \rightarrow n\pi^+$ are given and compared to results from other analyses.

PACS: 13.30.Eg, 13.40.Hq, 14.20.Gk

1 Introduction

The spectrum of baryon resonances is expected to be very rich and considerably more complex than the mesonic excitation spectrum. Yet, experimentally, the number of known light-quark mesons exceeds by far the number of known baryon resonances [1].

In quark models [2–4], most high-mass baryon resonances are only weakly coupled to $N\pi$ [5], and can thus not be seen in elastic πN scattering experiments. For inelastic reactions like $\pi N \rightarrow \eta N$, $\pi N \rightarrow K\Lambda$, $\pi N \rightarrow K\Sigma$, data with a polarized target are missing, and data on differential cross sections have low statistics, and are often inconsistent when different experiments are compared. States weakly coupled to the πN channel may thus have escaped identification. The situation was aggravated by a recent analysis of a large body of πN elastic and charge exchange scattering data in which many of the less established nucleon and Δ resonances were not confirmed [6].

Other interpretations of the baryon spectrum exist as well. Very popular are diquark models [7–10] in which one quark-pair is frozen and in which the number of predicted states decreases. Further, we mention approaches based on chiral Lagrangians in which low-lying baryon resonances are generated dynamically. In many cases, these calculations offer a consistent description of resonance properties and scattering data (see e.g. [11]) but so far, they do not give a survey of all resonances to be expected. Often discussed is the conjecture that chiral symmetry might be restored in high-mass meson and baryon resonances. [12, 13]. The conjecture gives an attractive interpretation of one experimental observation, that resonances show up as parity doublets or even higher multiplets. It fails to predict at which mass resonances should be found and, experimentally, all meson and baryon resonances on the leading

Regge trajectory have no parity partner. The AdS/QCD model describes QCD in terms of a dual gravitational theory [14, 15]; with some phenomenological adjustments, it is surprisingly successful in predicting the baryon mass spectrum and the number of expected states [16, 17]. It also predicts where parity multiplets should occur and where not. Reviews of baryon spectroscopy can be found in [18–20].

A decision which of the above approaches provides the most accurate representation of Nature requires a better experimental knowledge of the excitation spectrum. The limitations of the current data base on light-quark baryons is the stimulus for experiments studying baryon resonances in photoproduction of complex final states where the πN channel can be avoided in both the initial and the final state. The analysis of multibody final states including fermions is complex; in order to compare different approaches and to identify possible problems, a common meeting ground is needed. This is provided by the simplest photoproduction reactions, by $\gamma p \rightarrow p\pi^0$ and $\gamma p \rightarrow n\pi^+$. In this paper, we give masses, widths, photocouplings, and $N\pi$ decay branching ratios for the most important contributing resonances and compare our pion photoproduction and helicity amplitudes to those obtained by SAID [21], MAID [22] and within the Gießen model [23, 24]. The fits are based on a large number of data sets and include data with multibody final states. The study thus shows to which extent multibody final states are compatible with the best-studied $N\pi$ system.

2 Data used in the fits

A large number of reactions is used in the truly coupled-channel fits presented here. The data cover elastic πN

Table 1. Pion induced reactions fitted in the coupled-channel analysis and χ^2 contributions.

$\pi N \rightarrow \pi N$	Wave	N_{data}	w_i	χ^2/N_{data}
[6]	S_{11}	104	30	1.81
	S_{31}	112	20	2.27
	P_{11}	112	20	2.49
	P_{31}	104	20	2.01
	P_{13}	112	10	1.90
	P_{33}	120	10	2.53
	D_{13}	96	10	2.16
	D_{33}	108	12	2.56
	D_{15}	96	20	3.37
	F_{35}	62	20	1.32
	F_{37}	72	10	2.86
$\pi^- p \rightarrow \eta n$	Observ.	N_{data}	w_i	χ^2/N_{data}
[26]	$d\sigma/d\Omega$	70	10	1.96
[28]	$d\sigma/d\Omega$	84	30	2.67

scattering as well as inelastic reactions, they cover differential cross sections and single and double polarization variables. Reactions with multi-body final states are included exploiting an event-based likelihood method.

Different data sets often have a very different statistical power. Weights w_i are introduced to force the fit to take into account highly significant but low-statistics data, e.g. beam asymmetries. Without these weights, polarization data often have too small an impact on the fit result. The weight of a newly introduced data set is increased when the fit is visually unacceptable, or decreased until first discrepancies between data and fit become apparent.

2.1 Elastic $\pi N \rightarrow \pi N$ scattering

In the analysis presented here, data on elastic πN scattering (charge exchange is implicitly included) are not used directly. Instead, we rely on the detailed work of the George-Washington Center for Nuclear Studies [6] and use, for energies up to 2.2 GeV, their scattering amplitudes.

2.2 The reaction $\pi^- p \rightarrow \eta n$

The inelastic $\pi^- p$ scattering process leading to the $n\eta$ final state was reported from several experiments [25–28] and [29,30]. Above 1.8 GeV, large discrepancies between the data [27,30] show up. The data from [29] cover extreme backward angles and are partly incompatible with all other results. A critical discussion of the available data can be found in [31]. We use here the data from [26,28] (see Table 1) which show better consistency.

2.3 The reaction $\pi^- p \rightarrow \pi^0 \pi^0 n$

In the low-energy region, up to ~ 1.5 GeV in mass, very precise data from BNL are available [32]. These data are included in an event-based likelihood fit (see Table 2).

Table 2. Reactions leading to 3-body final states are included in event-based likelihood fits. The χ^2/N_{bin} values are calculated from selected Dalitz plots (see text for details). References to the data are given in the text.

$d\sigma/d\Omega(\pi^- p \rightarrow \pi^0 \pi^0 n)$		N_{data}	w_i	$-\ln L$
T=373 MeV		5248	10	-1025
T=472 MeV		10641	5	-2685
T=551 MeV	[32]	41172	2.5	-7322
T=655 MeV		63514	2	-15647
T=691 MeV		30030	3.5	-8256
T=733 MeV		29948	4	-7534
$d\sigma/d\Omega(\gamma p \rightarrow \pi^0 \pi^0 p)$	[33,34]	110601	4	-27568
$d\sigma/d\Omega(\gamma p \rightarrow \pi^0 \eta p)$	[35–37]	17468	8	-5587
$d\sigma/d\Omega(\pi^- p \rightarrow \pi^0 \pi^0 n)$		N_{bin}	χ^2/N_{bin}	
T=373 MeV		471	1.24	
T=472 MeV		478	1.30	
T=551 MeV	[32]	514	1.56	
T=655 MeV		518	1.31	
T=691 MeV		502	1.19	
T=733 MeV		501	1.53	
$d\sigma/d\Omega(\gamma p \rightarrow \pi^0 \pi^0 p)$	[33,34]	769	1.59	
$d\sigma/d\Omega(\gamma p \rightarrow \pi^0 \eta p)$	[35–37]	1119	1.04	
		N_{data}	w_i	χ^2/N_{data}
$\Sigma(\gamma p \rightarrow \pi^0 \pi^0 p)$	[38]	128	35	0.96
$\Sigma(\gamma p \rightarrow \pi^0 \eta p)$	[39]	180	15	2.37
$E(\gamma p \rightarrow \pi^0 \pi^0 p)$	[40]	16	35	1.91

The likelihood values have no direct significance; only likelihood difference can be related to probability changes when particular contributions are removed from the fit. To demonstrate the quality of the description we have constructed for every energy of the initial pion $m_{p\pi^0}^2$ versus $m_{p\pi^0}^2$ Dalitz plots for data and for Monte Carlo events with 40×40 bins. The Monte Carlo events were weighted with the squared amplitude from our final PWA solution. The data and weighted Monte Carlo Dalitz plots were compared; in Table 2 the χ^2/N_{bin} is given as well as the number of bins with nonzero number of Monte Carlo events.

2.4 Photoproduction of single neutral pions off protons

References to the data on the reaction $\gamma p \rightarrow p\pi^0$ and their χ^2 contributions are collected in Table 3. For the differential cross section, we use only the most recent data, reported by TAPS@MAMI [41], GDH-A2 [42,43], GRAAL [44], CB-ELSA [45,46], and CLAS [47] which cover a wide range of energies and angles. A large variety of older data exist which cover only a limited fraction of the energy and angular range. These data provide significant information on polarization observables.

The differential cross sections reported by the different collaborations exhibit small but significant systematic discrepancies practically in all mass regions; due to the small

Table 3. Observables from π and η photoproduction fitted in the coupled-channel analysis and χ^2 contributions. For pion production, free normalization factors and additional systematic errors were introduced to allow for data variation beyond statistical expectations (see text).

$\gamma p \rightarrow \pi^0 p$	Observ.	N_{data}	w_i	χ^2/N_{data}
[41] (TAPS@MAMI)	$d\sigma/d\Omega$	1692	1.5	1.25
[42, 43] (GDH A2)	$d\sigma/d\Omega$	164	7	1.34
[44] (GRAAL)	$d\sigma/d\Omega$	861	2	1.46
[45, 46] (CB-ELSA)	$d\sigma/d\Omega$	1106	3.5	1.34
[47] (CLAS)	$d\sigma/d\Omega$	592	5	2.11
[44, 48–55]	Σ	1492	3	3.26
[49–51, 56–65]	T	389	6	3.71
[49–51, 65–69]	P	607	3	3.23
[70, 71]	G	75	5	1.50
[70]	H	71	5	1.26
[42, 43]	E	140	7	1.23
[68, 72]	O_x	7	10	1.77
[68, 72]	O_z	7	10	0.46

$\gamma p \rightarrow \pi^+ n$	Observ.	N_{data}	w_i	χ^2/N_{data}
[73–82, 84–86]	$d\sigma/d\Omega$	1583	2	1.64
[43, 86] (GDH A2)	$d\sigma/d\Omega$	408	14	0.61
[87] (CLAS)	$d\sigma/d\Omega$	484	4	1.80
[55, 88–98]	Σ	899	3	3.48
[93, 94, 99–109]	T	661	3	3.21
[93, 94, 110]	P	252	3	2.90
[71, 111, 112]	G	86	3	5.64
[111–113]	H	128	3	3.90
[43, 86]	E	231	14	1.55

$\gamma p \rightarrow \eta p$	Observ.	N_{data}	w_i	χ^2/N_{data}
[114]	$d\sigma/d\Omega$	100	7	2.16
[116, 117]	$d\sigma/d\Omega$	680	40	1.47
[118]	Σ	51	10	2.26
[119]	Σ	100	15	2.02
[64]	T	50	70	1.48

statistical errors these are easily recognized. We show the systematic deviations by comparing the data with a curve representing the “first” fit to all data, without normalization factors.

In Fig. 1 the differential cross section from GDH-A2, CLAS and CB-ELSA are shown and compared to the preliminary fit for the 1495–1530 MeV mass range. The GDH data systematically exceed CLAS data while the CB-ELSA data provide numbers between these two measurements. The GDH-A2 data have a larger statistical error than the CLAS data; we introduced them into the fit with larger weight since they provide important information about the difference between helicity 3/2 and 1/2 cross sections.

In the mass region 1600–1750 MeV, there are notable discrepancies between GRAAL and CLAS data (here the CB-ELSA data fall again between GRAAL and CLAS results). As an example, the mass region around 1670 MeV is shown for the three data sets in Fig. 2. The curve cor-

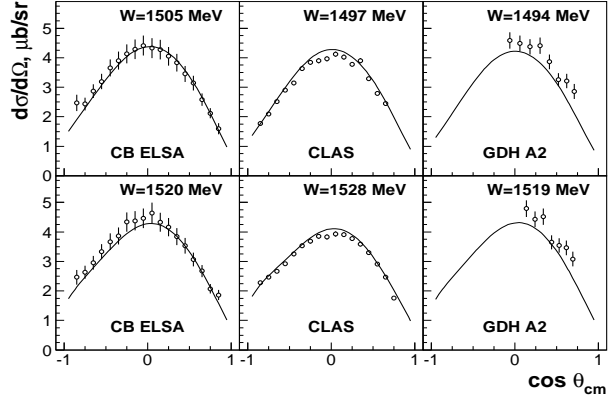


Fig. 1. The CB-ELSA, CLAS and GDH differential cross section on $\gamma p \rightarrow \pi^0 p$ in the region 1500 MeV. In the Crystal Barrel data, a common systematic error due to uncertainties in the reconstruction efficiency is included. The curve represents the “first” fit without normalization (see text). The GDH data are introduced with a large weight.

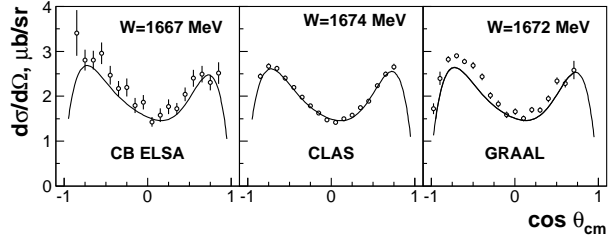


Fig. 2. Comparison of three data sets on the $\gamma p \rightarrow \pi^0 p$ differential cross section in the region 1670 MeV. The curve represents the “first” fit without normalization (see text).

responds to the fit where the CLAS data are taken with statistical errors only and dominate the solution.

At higher energies, only the CB-ELSA and CLAS data are available. There are two clear discrepancies between these data sets. The first one is located in the 1900 MeV mass region where the CB-ELSA data systematically exceed the CLAS data in the backward hemisphere (see Fig. 3, top). A second discrepancy shows up above $W = 2100$ MeV in the very forward angular range. Here the corresponding CB-ELSA points are systematically lower than those from CLAS. At $W=2300$ – 2400 MeV, the two data sets are fully consistent (see Fig. 3, bottom).

A fraction of the discrepancies is assigned to normalization. Most experiments give explicit normalization errors which were not taken into account in the “first” fit. We then allowed for a free normalization factor for the π^0 differential cross section, which is determined in the fit to 1.00 (TAPS@MAMI), 1.01 (GDH-A2), 0.99 (GRAAL and CB-ELSA) and 0.95 (CLAS).

The data from the four experiments are still not yet statistically compatible; at least one experiment must have additional unrecognized systematic errors. Of course, we do not know which experiment. We assume that all four experiments have systematic errors which were not recognized. These were estimated from the variance of the

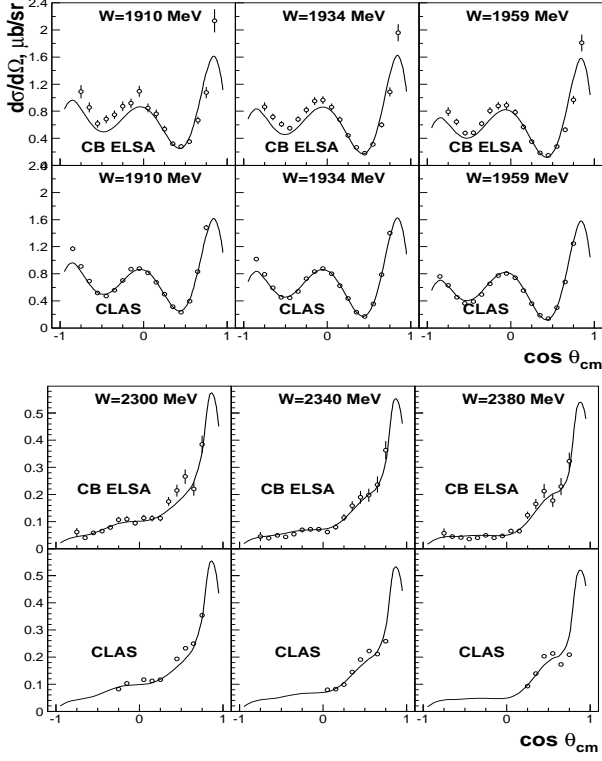


Fig. 3. The CB-ELSA and CLAS differential cross section on $\gamma p \rightarrow \pi^0 p$ in the region of 1900 (top) and 2350 (bottom) MeV. The curve represents the “first” fit without normalization (see text).

experimental results in preset bins of energy and angle (in $\cos \theta$). For this purpose, differential cross sections were calculated, by interpolation, for these bins. From the variance we estimated systematic errors which increase linearly from 1% at $W = 1400$ MeV to 9% at $W = 2450$ MeV. These systematic errors were added to all four data sets. With the increased systematic errors, the data are compatible and the χ^2 of a fit reflects the quality of a fit and not the inconsistency between different data sets. These errors are used in the fits only. In the figures, the data and their errors are shown as quoted in the original papers.

The beam asymmetry Σ has been determined in a number of experiments [44,48–55], as well as the target asymmetry T [49–51,56–64], and the polarization P of the recoiling proton [49–51,65–69]. Few data exist from experiments with polarized photons and polarized target or from measurements of the recoil polarization. Data on O_x and O_z can be found in [68,72], on G in [70,71], and on H in [70]. Data on the helicity difference $\sigma_{3/2} - \sigma_{1/2}$ were published in [42,43]; in Tables 2 and 3 we quote E which is defined as $(\sigma_{3/2} - \sigma_{1/2})/(\sigma_{3/2} + \sigma_{1/2})$. These data are included in the fits. Their statistical errors are mostly large, the systematic errors likely small. Hence we retain the original errors.

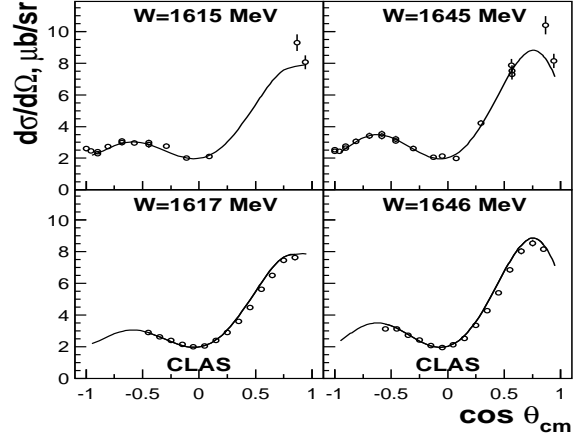


Fig. 4. Older data from different experiments (top) and CLAS differential cross section on $\gamma p \rightarrow \pi^+ n$ in the region 1630 MeV. The curve represents the “first” fit without normalization (see text). The consistency is excellent.

2.5 The reaction $\gamma p \rightarrow \pi^+ n$

Total cross sections were reported in [73–87]. Again, some discrepancies show up, at energies above 1600 MeV and in the forward region, between the new CLAS data and former measurements. An example of such discrepancies is given in Fig. 4. Normalization factors for the different data were introduced which are determined to be in the range from 0.96 to 1.03. A consistent description was achieved by adding a systematic error which increases linearly from 1% at $W = 1400$ MeV and to 9% at $W = 2450$ MeV.

The beam asymmetry Σ was determined in [55,88–98], the target asymmetry T in [93,94,99–109], the neutron recoil polarization can be found in [93,94,110]. A few data from double polarization are available: on G [71,111,112], H [111–113], and on the helicity difference $\sigma_{3/2} - \sigma_{1/2}$ [43,86]. The data are fitted with the errors as given in the respective papers.

2.6 Photoproduction of η mesons off protons

For photoproduction of η mesons, differential cross sections [114–117,119] and the related beam asymmetry Σ [118–120] are the only quantities which have been measured so far. Double polarization observables are presently studied intensively at several laboratories but so far, no results have been published. The recent high-statistics measurements on $\gamma p \rightarrow p\eta$ [121,122] are not yet included in the fits presented here.

2.7 The reactions $\gamma p \rightarrow K^+ \Lambda, K^+ \Sigma^0$ and $K^0 \Sigma^+$

Data on hyperon photoproduction used in the present fits are collected in Table 4. We use the differential cross sections for $\gamma p \rightarrow K^+ \Lambda$ and $K^+ \Sigma^0$ from CLAS [123]. As shown in [124], the Saphir data [125] on differential cross sections are about compatible with the CLAS data when

Table 4. Hyperon photoproduction observables fitted in the coupled-channel analysis and χ^2 contributions.

$\gamma p \rightarrow K^+ \Lambda$	Observ.	N_{data}	w_i	χ^2/N_{data}
[123]	$d\sigma/d\Omega$	1377	4	1.81
[126]	Σ	45	10	1.65
[127]	Σ	66	5	1.53
[128]	P	202	6.5	2.03
[127]	P	66	3	1.26
[129]	T	66	15	1.26
[130]	C_x	160	11	1.23
[130]	C_z	160	11	1.41
[129]	O_x	66	12	1.30
[129]	O_z	66	15	1.54
<hr/>				
$\gamma p \rightarrow K^+ \Sigma$	Observ.	N_{data}	w_i	χ^2/N_{data}
[123]	$d\sigma/d\Omega$	1280	2.5	2.06
[126]	Σ	45	10	1.11
[127]	Σ	42	5	0.90
[128]	P	95	6	1.45
[130]	C_x	94	7	2.20
[130]	C_z	94	7	2.00
<hr/>				
$\gamma p \rightarrow K^0 \Sigma^+$	Obsv.	N_{data}	w_i	χ^2/N_{data}
[128]	$d\sigma/d\Omega$	48	2.3	3.76
[131]	$d\sigma/d\Omega$	160	5	0.98
[132]	$d\sigma/d\Omega$	72	5	0.82
[132]	P	72	20	0.61

an energy dependent normalization factor is introduced. The beam asymmetry was measured at SPring-8 [126] and GRAAL [127]; the Λ polarization was deduced in [127] and [128]. Target asymmetry T and O_x and O_z for $\gamma p \rightarrow K^+ \Lambda$ were reported in [129]. In [130], CLAS data on the spin transfer coefficients C_x and C_z were presented for both, $\gamma p \rightarrow K^+ \Lambda$ and $\gamma p \rightarrow K^+ \Sigma^0$.

Differential cross sections on the reaction $\gamma p \rightarrow K^0 \Sigma^+$ were measured by CLAS [128], Saphir [131] and CB-ELSA/TAPS [132]. For the latter data we include the determination of the P polarization derived from an analysis of the Σ^+ decay.

2.8 The reactions $\gamma p \rightarrow p\pi^0\pi^0$ and $\gamma p \rightarrow p\pi^0\eta$

The two reactions $\gamma p \rightarrow p\pi^0\pi^0$ [33,34] and $\gamma p \rightarrow p\pi^0\eta$ [35–37] are included event by event using an extended likelihood method. The quality of the fit can be judged from the description of Dalitz plots. For the $\gamma p \rightarrow p\pi^0\pi^0$ reaction we constructed Dalitz plots in $m_{p\pi^0}^2$ versus $m_{p\pi^0}^2$ with 20×20 bins, for the four 100 MeV γp invariant mass intervals from 1350 to 1750 MeV. For the $\gamma p \rightarrow p\eta\pi^0$ reaction, $m_{p\pi^0}^2$ versus $m_{p\eta}^2$ Dalitz plots were constructed for seven 100 MeV γp invariant mass intervals from 1700 to 2400 MeV. The number of bins with nonzero Monte Carlo events and χ^2/N_{bin} are given in Table 2. The beam asymmetries [38,39] and the helicity dependence E [40] are included in the fit in the form of histograms.

Both these reactions have been studied intensively, see [133–146] for the first and [147–149] for the latter reaction. For these data only selected histograms are available; they are not included in our fits.

3 Partial wave amplitudes

A general expression for the decomposition of the two-particle scattering amplitude $A(s, t)$ into partial wave amplitudes $A_n^{\beta\beta'}(s)$ which describe production, propagation and decay of a two-particle systems with fixed total angular momentum J , parity and (if conserved) C -parity can be written as:

$$A(s, t) = \sum_{\beta\beta'n} A_n^{\beta\beta'}(s) Q_{\mu_1 \dots \mu_n}^{(\beta)\dagger}(k) F_{\nu_1 \dots \nu_n}^{\mu_1 \dots \mu_n} Q_{\nu_1 \dots \nu_n}^{(\beta')}(q) \quad (1)$$

where k_i are initial and q_i are final particle momenta, $s = (k_1 + k_2)^2 = (q_1 + q_2)^2 = P^2$, $t = (k_1 - q_1)^2 = (k_2 - q_2)^2$, $k = (k_1 - k_2)/2$, $q = (q_1 - q_2)/2$ and $n = J$ for a boson system and $n = J - 1/2$ for a fermion one. The vertices $Q_{\nu_1 \dots \nu_n}^{(\beta)}$ and $Q_{\mu_1 \dots \mu_n}^{(\beta)\dagger}$ (' \dagger ' stands for hermitian conjugation) describe the transition of the system into the initial- and final-state particles, and depend on the total and relative momenta. The indices β and β' list quantum numbers of the production and decay amplitudes, e.g. isospin, spin and orbital angular momenta. The tensor $F_{\nu_1 \dots \nu_n}^{\mu_1 \dots \mu_n}$ depends only on the total momentum P and describes the tensor structure of the partial wave. It is often called projection operator. The formalism for construction of vertices for meson-baryon partial waves and projection operators is given in [150,151]. For convenience we provide key formula for projection operators and vertices in Appendix A.

In the case of resonance production, the total amplitude $A(s, t)$ can be expanded into a sum of partial wave amplitudes multiplied by vertices, see eq. (1). Here the partial wave amplitudes $A_n^{\beta\beta'}(s)$ provide the energy dependence of the resonance which can be parameterized, for example, as N/D amplitude, as K -matrix or, in the simplest case, as a Breit-Wigner amplitude [152]. For non-resonant contributions, like t and u channel exchanges, the situation is different. In many partial wave analyses (including the present one) these contributions are simply added to the resonant part of the total amplitude and the sum is used to fit the experimental data. However, one needs to know the contribution of t and u -exchanges in every partial wave if the final partial wave amplitudes are to be compared with results from other analyses. This decomposition is also required when rescattering between non-resonant and resonant parts of the amplitude should be taken into account. For the non-resonant contributions used in the energy dependent fits one has therefore to solve an inverse task: to extract partial wave amplitudes from the total amplitude.

This task can be solved by using the orthogonality condition for partial wave operators. Multiplying the total amplitude from eq. (1) with initial and final projection operators and vertices and integrating over solid angle of

the initial and final momenta we obtain

$$F_{\mu_1 \dots \mu_n}^{\tau_1 \dots \tau_n} \int \frac{d\Omega_k}{4\pi} \frac{d\Omega_q}{4\pi} Q_{\mu_1 \dots \mu_n}^{(\alpha)}(k) A(s, t) Q_{\nu_1 \dots \nu_n}^{(\alpha')}(q) F_{\eta_1 \dots \eta_n}^{\nu_1 \dots \nu_n} \\ = (-1)^n F_{\eta_1 \dots \eta_n}^{\tau_1 \dots \tau_n} \sum_{\beta\beta'} A_n^{\beta\beta'}(s) W_n^{\alpha\beta}(k_\perp^2) W_n^{\beta'\alpha'}(q_\perp^2), \quad (2)$$

where k_\perp^2 and q_\perp^2 are squared relative momenta orthogonal to the total momentum of the system P (see Appendix A).

The factor $W_n^{\alpha\beta}$ corresponds to the on-shell one-loop amplitude for transition between two vertices $Q_{\mu_1 \dots \mu_n}^{(\beta)}$. It can be calculated as

$$W_n^{\alpha\beta}(k_\perp^2) = \frac{F_{\mu_1 \dots \mu_n}^{\alpha_1 \dots \alpha_n}}{\xi_n} \int \frac{d\Omega_k}{4\pi} Q_{\mu_1 \dots \mu_n}^{(\alpha)}(k) Q_{\nu_1 \dots \nu_n}^{(\beta)}(k) F_{\alpha_1 \dots \alpha_n}^{\nu_1 \dots \nu_n} \\ \xi_n = (-1)^n F_{\mu_1 \dots \mu_n}^{\nu_1 \dots \nu_n} g_{\mu_1 \nu_1} \dots g_{\mu_n \nu_n}. \quad (3)$$

For meson-nucleon and γN vertices, the $W_n^{\alpha\beta}$ were calculated in [151]. For convenience we provide the corresponding expressions in Appendix B and expressions for partial wave amplitudes for photoproduction of a single meson are given in Appendix C.

3.1 Parameterization of the partial wave amplitudes

In the present analysis, the partial waves at low energies are described in the framework of a K-matrix/P-vector approach. High-mass resonances (above 2.2 GeV) are described by relativistic multi-channel Breit-Wigner amplitudes. In the case of photoproduction reactions, the reggeized t- and u-channel amplitudes were added to the resonant part. Then the multipoles were calculated by solving eq. (2).

3.1.1 Pion induced reactions in K-matrix approach

The multi-channel amplitude is given by the matrix $\hat{\mathbf{A}}(s)$ where the matrix element $A_{ab}(s)$ defines the transition amplitude from state 'a' to state 'b'. In eq. (1) this amplitude is denoted as $A_n^{\beta\beta'}(s)$ to emphasize the different spin-parity contributions. Now we will use the notation $A_{ab}(s)$ which identifies the initial and the final channels, e.g. γN , πN , ηN , $K\Lambda$, $\pi\Delta$, and omit the indices representing the partial wave. Scattering between different channels is taken into account explicitly in the K-matrix; the amplitude is given by

$$\hat{\mathbf{A}}(s) = \hat{\mathbf{K}} (\hat{\mathbf{I}} - i\hat{\rho}\hat{\mathbf{K}})^{-1}. \quad (4)$$

where $\hat{\mathbf{K}}$ is the K-matrix, $\hat{\mathbf{I}}$ is the unity matrix and $\hat{\rho}$ is a diagonal matrix of the according phase space. For two-particle states (for example πN), the phase space is calculated as a simple loop diagram (see [151]). For $J = L + 1/2$, the so-called '+' states, the phase space is equal to

$$\rho_+(s) = \frac{\alpha_L}{2L+1} \frac{2|\mathbf{k}|^{2L+1}}{\sqrt{s}} \frac{k_{10} + m_N}{2m_N} \frac{F(k^2)}{B(L, r, k^2)} \quad (5)$$

and for '-' states with $J = L - 1/2$, the phase space is given by

$$\rho_-(s) = \frac{\alpha_L}{L} \frac{2|\mathbf{k}|^{2L+1}}{\sqrt{s}} \frac{k_{10} + m_N}{2m_N} \frac{F(k^2)}{B(L, r, k^2)} \quad (6)$$

where s is the total energy squared, k , is the relative momentum between baryon and meson, \mathbf{k} its three-vector component, k_{10} is the energy of the baryon (with mass m_N) calculated in the c.m.s. of the reaction. J is the total, L the orbital angular momentum of the baryon-plus-meson system, and the coefficient α_L is equal to:

$$\alpha_L = \prod_{n=1}^L \frac{2n-1}{n}. \quad (7)$$

The phase volume is regularized at large energies by a standard Blatt-Weisskopf form $B(L, r, k^2)$ with $r = 0.8$ fm, and a form-factor $F(k^2)$ of the type

$$F(k^2) = \frac{\Lambda + 0.5}{\Lambda + k^2} \quad \text{or} \quad F(k^2) = \frac{\Lambda + 2.5}{\Lambda + s}. \quad (8)$$

Fits with both parameterizations yield nearly identical results. The parameter Λ were taken from our previous analysis [124, 153] and fixed to 1.5 for the first parameterization and 3.0 for the second one. The exact formulas for the three-body phase volume are given in [151].

The K-matrix $\hat{\mathbf{K}}$ is parameterized as follows:

$$K_{ab} = \sum_{\alpha} \frac{g_a^{(\alpha)} g_b^{(\alpha)}}{M_{\alpha}^2 - s} + f_{ab}, \quad (9)$$

where M_{α} and $g_a^{(\alpha)}$ are the mass and the coupling constant of the resonance α , and where f_{ab} describes a direct (non-resonant) transition from the initial state a to the final state b , e.g. from $\pi N \rightarrow \Lambda K$.

For most partial waves it is sufficient to assume that f_{ab} are constants. The S_{11} and S_{31} and waves require a slightly more complicated structure, we use

$$f_{ab} = \frac{f_{ab}^{(1)} + f_{ab}^{(2)} \sqrt{s}}{s - s_0^{ab}}. \quad (10)$$

Here the $f_{ab}^{(i)}$ and s_0^{ab} are constants which are determined in the fits. In the case of the S_{11} wave, this more flexible parameterization is required to describe $\pi N \rightarrow N\pi$, $\pi N \rightarrow N\eta$, and $\eta N \rightarrow N\eta$ transitions. Let us note that this form is similar to the one used by SAID [6].

3.1.2 The photoproduction amplitude

The photoproduction amplitude can be written in the P-vector approach [154]. The P-vector amplitude for the initial state 'a' photoproduction is then given by

$$A_a = \hat{P}_b (\hat{I} - i\hat{\rho}\hat{K})_{ba}^{-1}. \quad (11)$$

The production vector $\hat{\mathbf{P}}$ is parameterized as:

$$P_b = \sum_{\alpha} \frac{g_{\gamma N}^{(\alpha)} g_b^{(\alpha)}}{M_{\alpha}^2 - s} + \tilde{f}_b \quad (12)$$

where $g_{\gamma N}^{(\alpha)}$ are the photo-couplings of the resonance α and where non-resonant production of a final state b is described by contributions \tilde{f}_b . In general, these are functions of s but mostly, a constant \tilde{f}_b is sufficient.

The P-vector approach is based on the idea that a channel with a weak coupling can be omitted from the K-matrix. Indeed, adding to the K-matrix the γN channel would not change the properties of the amplitude. Due to its weak coupling, the γN interaction can be taken into account only once; this is done in the form of a P-vector. Loops due to virtual decays of a resonance into $N\gamma$ and back into the resonance can be neglected safely. A similar approach can be used to describe decay modes with a weak couplings. The amplitude for the transition into such a channel can be written as D-vector amplitude,

$$A_a = \hat{D}_a + [\hat{K}(\hat{I} - i\hat{\rho}\hat{K})^{-1} \hat{\rho}]_{ab} \hat{D}_b, \quad (13)$$

where the parameterization of the D-vector is similar to the parameterization of the P-vector:

$$D_b = \sum_{\alpha} \frac{g_b^{(\alpha)} g_f^{(\alpha)}}{M_{\alpha}^2 - s} + \tilde{d}_b. \quad (14)$$

Here $g_f^{(\alpha)}$ is the coupling of a resonance to the final state and \tilde{d}_b is a non-resonant production from the K-matrix-channel b to the final state. As in the case of the P-vector approach, channels with weak couplings can be taken into account only in their final decay, and are not taken into account in the rescattering. Let us note that if the final state is already included as one of K-matrix channels, the amplitude (13) reproduces the K-matrix amplitude (4).

In cases where both, initial and final coupling constants are weak, we use an approximation which we call PD-vector. In this case the amplitude is given by

$$A_{ab} = \hat{G}_{ab} + \hat{P}_a(\hat{I} - i\hat{\rho}\hat{K})^{-1} \hat{\rho} \hat{D}_b, \quad (15)$$

where \hat{G}_{ab} corresponds to a tree diagram for the transition from state 'a' to state 'b'.

$$G_{ab} = \sum_{\alpha} \frac{g_a^{(\alpha)} g_b^{(\alpha)}}{M_{\alpha}^2 - s} + \tilde{h}_{ab}. \quad (16)$$

Here $g_i^{(\alpha)}$ is the production coupling of the resonance. For photoproduction, $g_a^{(\alpha)} = g_{\gamma N}^{(\alpha)}$ holds true, and \tilde{h}_{ab} is the direct non-resonant transition from the initial to the different final channels.

3.2 Reggeized meson exchange amplitudes

At high energies, angular distributions of photo-produced mesons exhibit clear peaks in the forward direction. These

peaks originate from meson exchanges in the t-channel. Their contributions are parameterized as π , $\rho(\omega)$, K or K^* exchanges.

The most straight forward parameterization of particle exchange amplitudes is the exchange of Regge trajectories. The invariant part of the t-channel exchange amplitude can be written as [152]

$$T(s, t) = g_1(t) g_2(t) R(\pm, \nu, t) \quad \nu = \frac{1}{2}(s - u). \quad (17)$$

Here, g_i are vertex functions, and $R(+, \nu, t)$ and $R(-, \nu, t)$ are Reggeon propagators for exchanges with positive and negative signature. Exchanges of π and K have positive, ρ , ω and K^* exchanges have negative signature.

The ρ trajectory has a negative signature and the corresponding propagator is equal to

$$R_{\rho}(-, \nu, t) = \frac{ie^{-i\frac{\pi}{2}\alpha_{\rho}(t)}}{\cos(\frac{\pi}{2}\alpha_{\rho}(t))\Gamma\left(\frac{\alpha_{\rho}(t)}{2} + \frac{1}{2}\right)} \left(\frac{\nu}{\nu_0}\right)^{\alpha_{\rho}(t)}. \quad (18)$$

where $\alpha_{\rho}(t) = 0.50 + 0.85t$. The ω trajectory is identical to the ρ trajectory. The expressions for other Reggeon propagators used in the fit are given in Appendix D.

4 Partial wave analysis

4.1 Fit of the $\pi^0 p$ and $\pi^+ n$ photoproduction reactions

The new CLAS data on the $\gamma p \rightarrow \pi^0 p$ reaction are compared to our fit in Fig. 5. The χ^2 contributions of this fit from the various channels are given in Tables 1-4. We remind the reader that we estimated additional systematic errors for the $\gamma p \rightarrow \pi^0 p$ and $\gamma p \rightarrow \pi^+ n$ differential cross sections; these additional errors are not shown in Fig. 5.

Some systematic deviations between data and fit can be recognized in the mass region below 1800 MeV. These are mostly the result of discrepancies between the data. In Fig. 6 we show for comparison some CB-ELSA data, and in Fig. 7 some GRAAL data, for invariant masses which are close to the CLAS values. At higher energies the solution describes very well the new CLAS data, however CB-ELSA data are also described with rather good accuracy.

The new data on the $\gamma p \rightarrow \pi^+ n$ and the fit curve are shown in Fig. 8. Here, the total normalization factors resolve rather well discrepancies at masses below 1600 MeV. The description of the earlier data on the $\gamma p \rightarrow \pi^+ n$ in this mass region is shown in Fig. 9.

4.2 Photoproduction multipoles

We now turn to a discussion of the partial wave amplitudes. It should be stressed that the amplitudes we give for $\gamma p \rightarrow p\pi^0$ and $\gamma p \rightarrow n\pi^+$ are constrained by a large number of other reactions. This is particularly important

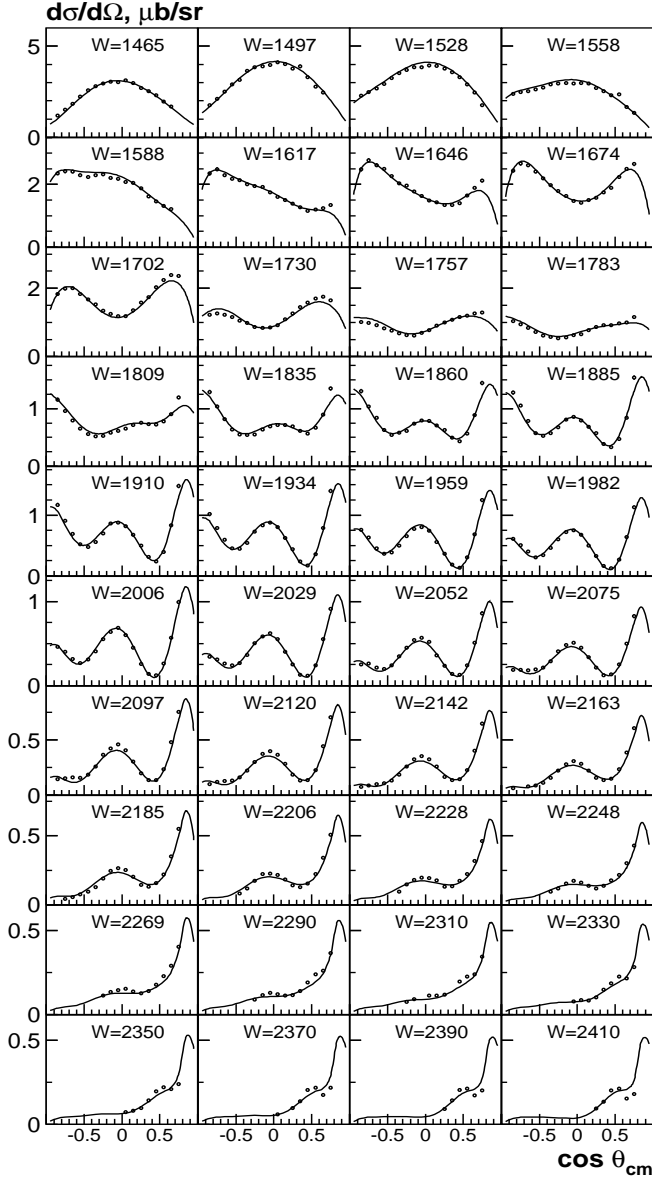


Fig. 5. CLAS data on the differential cross section for $\gamma p \rightarrow \pi^0 p$ with current solution. Only statistical errors for the CLAS data are shown

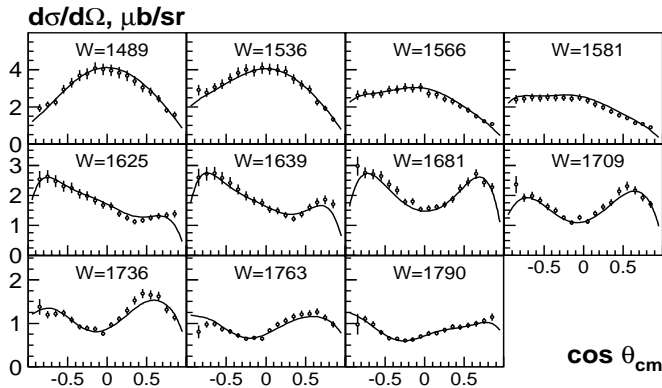


Fig. 6. CB-ELSA data on the $\gamma p \rightarrow \pi^0 p$ differential cross section for energies below 1.8 GeV. Only the errors quoted by the CB-ELSA collaboration are shown.

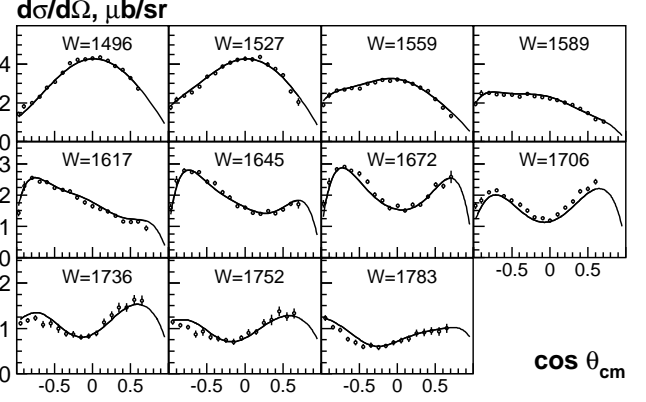


Fig. 7. GRAAL data on the $\gamma p \rightarrow \pi^0 p$ differential cross section at energies close to the CLAS values. Only the errors quoted by the GRAAL collaboration are shown.

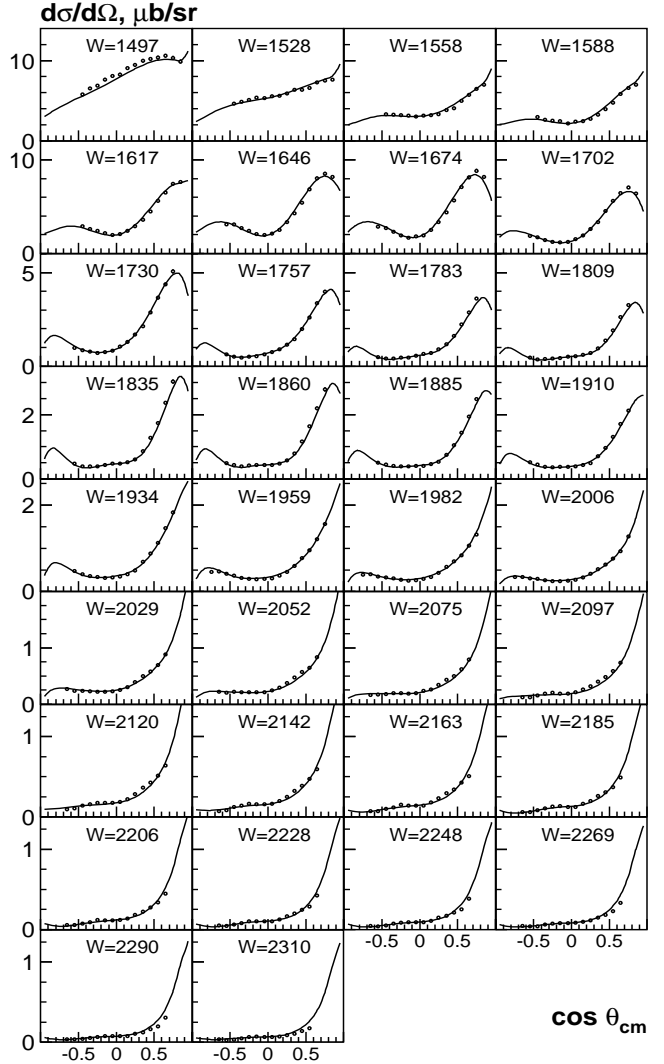


Fig. 8. CLAS data on the $\gamma p \rightarrow \pi^+ n$ differential cross section with the current solution.

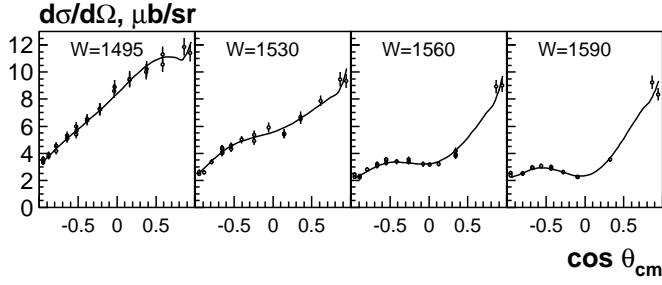


Fig. 9. The $\gamma p \rightarrow \pi^+ n$ differential cross section with the current solution. The data are taken from [75, 77–82, 85]

in the vicinity of thresholds. Of course, the elastic πN scattering amplitude and the pion photoproduction amplitude are influenced by opening new channels and the couplings to the new channels can be estimated from their effect on the scattering and photoproduction amplitudes. But this is rather indirect, and it is desirable to take the inelastic channels into account directly.

The multipoles for π^0 photoproduction are shown in Fig. 12 in comparison to the SAID SP09K2700 [21] and MAID 2007 [22] solutions, those for $\gamma p \rightarrow \pi^+ n$ in Fig. 13. The errors cover a large number of fits which differ mostly by the parameterization of the $2\pi N$ channel at masses above 1.8 GeV. For convenience of the reader, we list in Table 5 the lowest photoproduction multipoles and the corresponding partial waves.

Most amplitudes derived within the SAID, MAID, or BnGa approach yield consistent results, at least qualitatively. The best agreement is found for the M_1^+ amplitude which describes the spin flip amplitude for the photo-induced transition from the proton to the Δ resonance and its excitations. The Δ resonance is fully elastic, hence the agreement in the low-mass region is not unexpected. Even the small E_1^+ multipoles are not inconsistent. Some multipoles which we discuss next show significant differences between the different approaches. The E_0^+ multipole has a similar structure in all three approaches but shows significant differences in detail. In the BnGa solution, the electric dipole transition E_0^+ exceeds the other solutions in the threshold regions, likely due to a larger role of the sub-threshold ΔK^+ amplitude. The differences are even larger for the M_1^- multipole; this may be not unexpected in view of the notorious difficulties with the $1/2^+$ partial wave.

Table 5. Photoproduction multipoles and partial waves. In general, two multipoles lead to one spin-parity wave.

Multipoles	Partial waves		J^P	
E_0^+	-	S_{11}	S_{31}	$1/2^-$
-	M_1^-	P_{11}	P_{31}	$1/2^+$
E_1^+	M_1^+	P_{13}	P_{33}	$3/2^+$
E_2^-	M_2^-	D_{13}	D_{33}	$3/2^-$
E_2^+	M_2^+	D_{15}	D_{35}	$5/2^-$
E_3^-	M_3^-	F_{15}	F_{35}	$5/2^+$

Surprisingly, the multipoles for $\gamma p \rightarrow n\pi^+$ are in much better consistency. The differences in the E_2^- and M_2^- can be assigned to additional $\Delta_{3/2^-}(1940)$ and $\Delta_{3/2^-}(2260)$ resonances introduced to fit data on $\gamma p \rightarrow p\pi^0\eta$ [36, 37]. Significantly different are the multipoles leading to $5/2^-$ states. In our fits, the E_2^+ and M_2^+ multipoles include an additional resonance $N_{5/2^-}(2060)$ [153]. We note that the (dominant) resonance contributions are compatible with the Watson theorem.

4.3 Properties of contributing resonances

A large number of resonances is identified in the fits. Some have a strong coupling to pion photoproduction, for others, the product of squared photocoupling constant and $N\pi$ decay branching ratio is small and they contribute mostly to inelastic channels; their properties will be discussed elsewhere. These latter resonances are listed in Table 6. They do help to improve the fit to pion photoproduction but their helicity amplitudes are not well defined, and photo-couplings and decay branching ratios of these states can be varied within large limits without significant χ^2 deterioration. All these solutions were included in the error estimation procedure.

The pole position of the states, photo-couplings and πN branching ratios for the states contributing strongly to pion photoproduction are given in Table 7. The inclusion of the new CLAS data rather notably stabilized the solution and improved most of the errors. The pole positions are determined by finding zeros of the real and the imaginary part of the denominator in the partial wave amplitudes. Thus two lines are defined in the complex energy plane. Their crossing points defines the pole position. The coupling constants, including the helicity amplitudes, are calculated as residues of the P-vector/K-matrix amplitude at the pole position and are given together with their phases. The πN branching ratios are calculated as squared residue-couplings, multiplied by the phase volume taken at the Breit-Wigner resonance mass. We note that nucleon-meson or nucleon-photon couplings are defined at the pole position of a resonance, and are complex numbers. In Table 7 we give the (complex) photon-couplings at the pole positions; their analogues, the helicity amplitudes $A_{1/2}$ and $A_{3/2}$ are defined for Breit-Wigner amplitudes, not for more general formalisms. The method how we derive Breit-Wigner parameters and helicity amplitudes is discussed below. For the $P_{13}(1720)$ and $D_{33}(1700)$ resonances, the Breit-Wigner width is much larger than one might expect from the pole position. In the $N\pi$ channel, the visible width is much closer to this expectation. The effect is known from $a_0(980)$ which has a visible width of about 50 MeV in the $\pi\eta$ mass distribution but a much larger width in the $K\bar{K}$ mass distribution the width is much larger because of the rapidly opening $K\bar{K}$ phase space. In the $P_{13}(1720)$ and $D_{33}(1700)$ case, the phase space for $N\pi\pi$ 3-body decays grows rapidly with increasing mass.

Within the quoted errors, the results from the new solution are mostly compatible with those published in

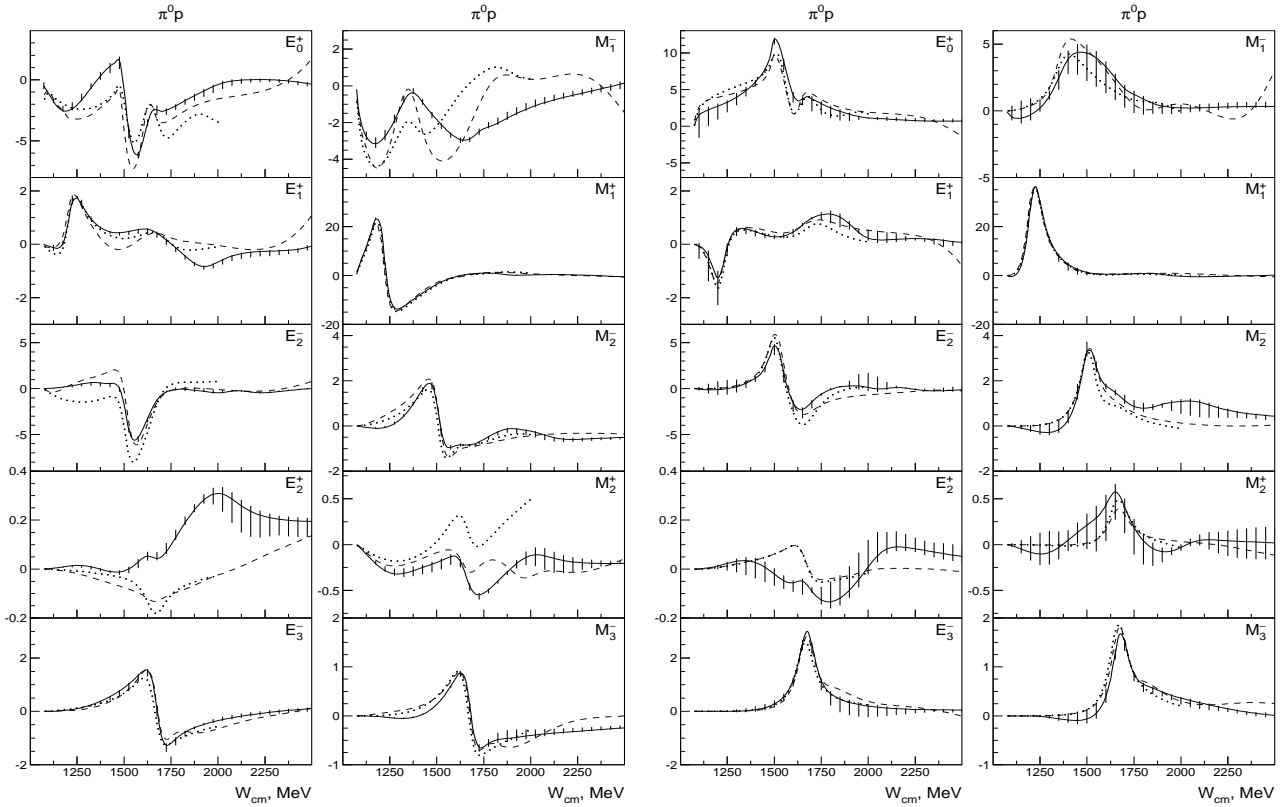


Fig. 10. The real (two left-hand columns) and imaginary (two right-hand columns) part of multipoles for the π^0 photoproduction. The errors are systematic and cover a large number of fits (see the text). The dashed curves correspond to the SAID solution SP09K2700 [21] and the dotted curves to the MAID solution 2007 [22]

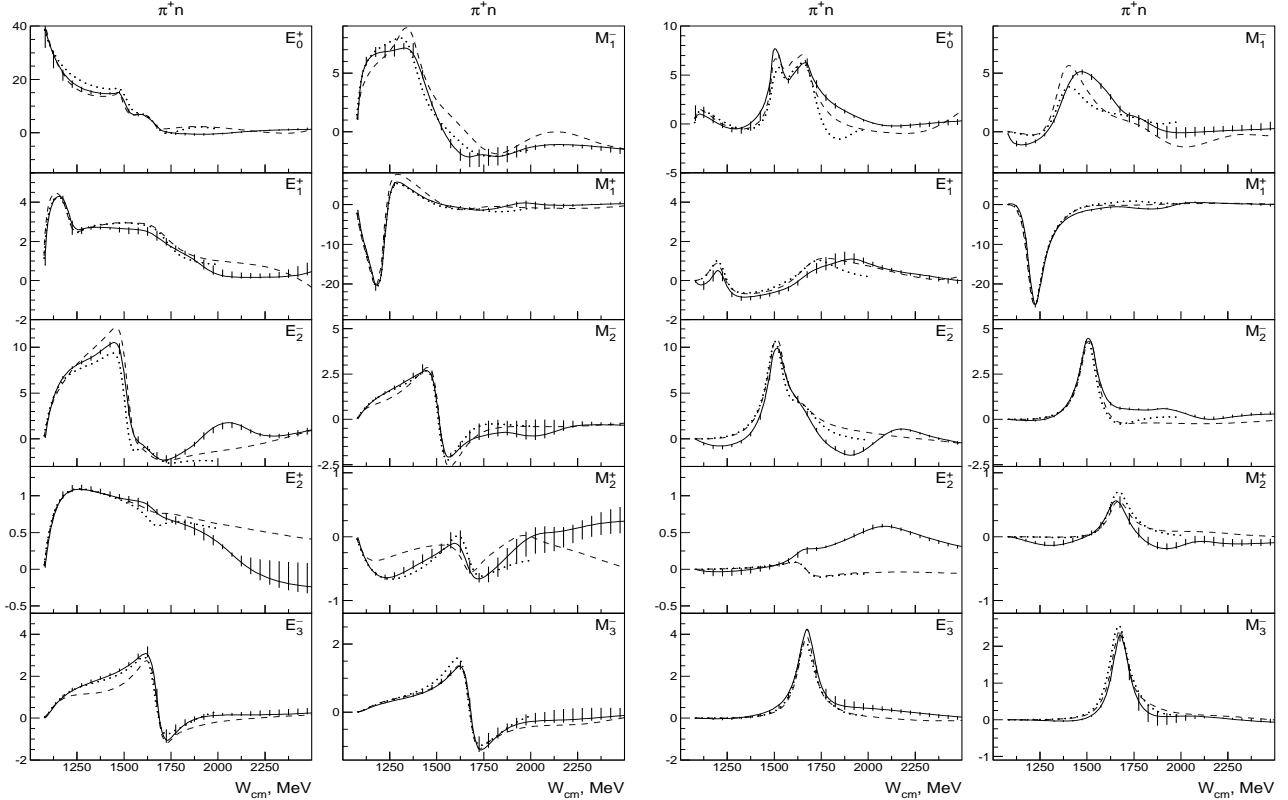


Fig. 11. The real (two left-hand columns) and imaginary (two right-hand columns) part of multipoles for the $\gamma p \rightarrow \pi^+ n$ reaction. The errors are systematic and cover a large number of fits (see the text). The dashed curves correspond to the SAID solution SP09K2700 [21] and the dotted curves to the MAID solution 2007 [22].

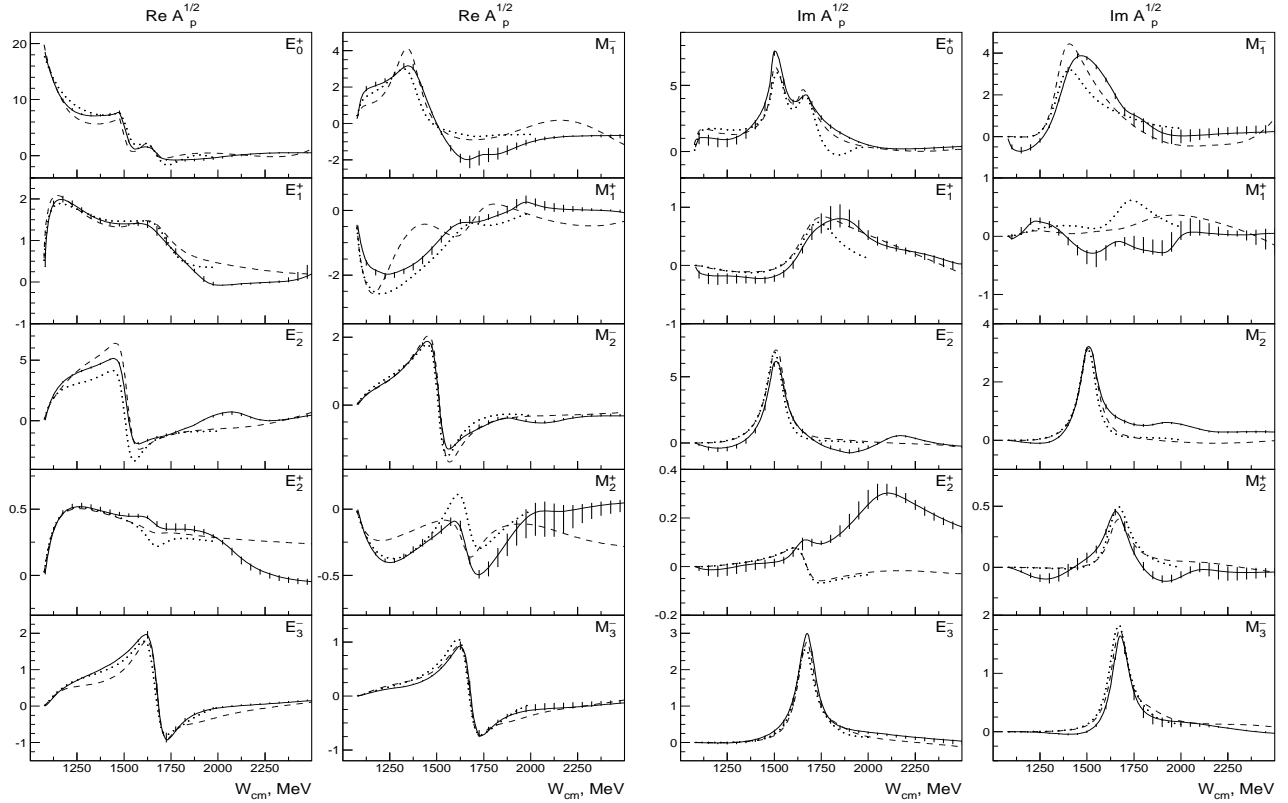


Fig. 12. The real (two left-hand columns) and imaginary (two right-hand columns) part of the isospin-1/2 photoproduction multipoles. The errors are systematic and cover a large number of fits (see the text). The dashed curves correspond to the SAID solution SP09K2700 [21] and the dotted curves to the MAID solution 2007 [22]

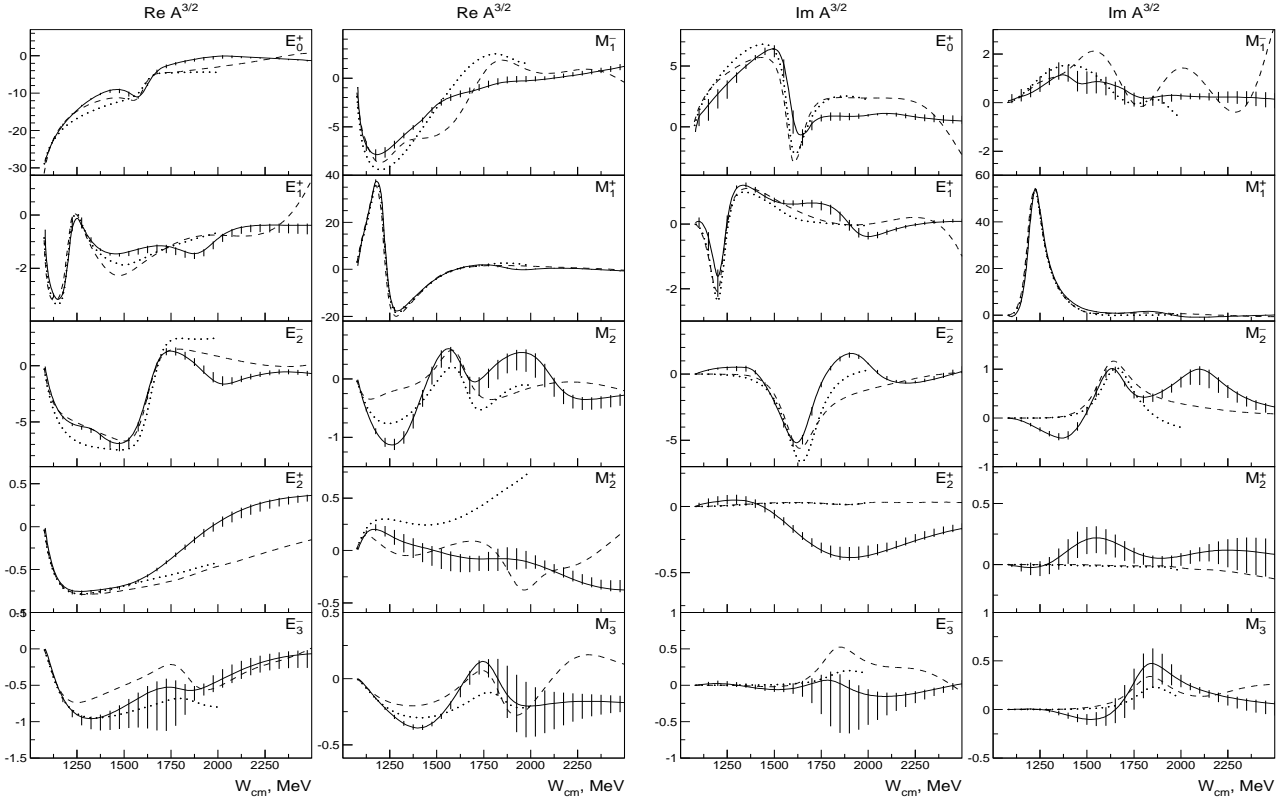


Fig. 13. The real (two left-hand columns) and imaginary (two right-hand columns) part of the isospin-1/2 photoproduction multipoles. The errors are systematic and cover a large number of fits (see the text). The dashed curves correspond to the SAID solution SP09K2700 [21] and the dotted curves to the MAID solution 2007 [22].

Table 6. Baryon resonances included in the fit which contribute little to photoproduction of pions.

	Mass	Width		Mass	Width
$P_{11}(1860)$	1900 ± 30	300 ± 40	$P_{13}(1900)$	1960 ± 30	185 ± 40
$D_{13}(1700)$	1730 ± 40	310 ± 60	$D_{13}(1875)$	1870 ± 25	150 ± 40
$P_{33}(1600)$	1640 ± 40	480 ± 100	$P_{33}(1920)$	1950 ± 40	330 ± 50
$F_{15}(2000)$	1910 ± 50	360 ± 80	$D_{15}(2070)$	2065 ± 25	340 ± 40
$D_{33}(1940)$	1995 ± 40	360 ± 50	$D_{13}(2170)$	2160 ± 35	370 ± 50
$D_{33}(2360)$	2360 ± 50	480 ± 80	$S_{31}(1900)$	1955 ± 30	335 ± 40

[33]. The largest changes to our previous solution are observed for the photo-couplings of the $S_{31}(1620)$ resonance (which was $(130 \pm 50) \text{ GeV}^{-1/2} \times 10^3$ in [33]), and for the small helicity component $A_{1/2}$ of the $D_{13}(1520)$ (which was $(7.0 \pm 1.5) \text{ GeV}^{-1/2} \times 10^3$). The changes are largely due to the inclusion of additional polarization data for $\gamma p \rightarrow \pi^0 p$ and $\gamma p \rightarrow \pi^+ n$.

The new data also require $P_{11}(1710)$. In [34], this resonance improved the description of the data slightly but we were not forced to introduce it. In the present fit, there are three resonances above the nucleon in the P_{11} wave: the Roper resonance $P_{11}(1440)$, the $P_{11}(1710)$, and the newly proposed $P_{11}(1860)$.

We found two minima for the photo-couplings of the $F_{35}(1905)$ state. Both solutions are given in the Table 7 (5th and 6th row, 2nd column). The first solution corresponds well to the PDG average values, while the second solution has an almost vanishing helicity-3/2 coupling. Both solutions reproduce single meson photoproduction data with the same quality, however the second solution provides a better likelihood for the $\gamma p \rightarrow \pi^0 \eta p$ reaction. The analysis of the high energy data on the two-pion photoproduction will help to define which solution is the physical one. Also the forthcoming double polarization data will provide new and important constraints on the amplitudes.

The pole structure of two resonances is found to be ambiguous. The pole of the $S_{11}(1650)$ resonance is located between the ΛK and ΣK thresholds. In one set of acceptable solutions we found large couplings of this state to these channels and a complicated pole structure of two or even more poles close to the two thresholds. We included such pole positions and corresponding residues in the errors given in Table 7. The forthcoming analysis of the data on the $\pi p \rightarrow K \Lambda$ should help to define the S_{11} pole structure more accurately, however new data on $\pi N \rightarrow K \Lambda$ and $\pi N \rightarrow K \Sigma$ would be extremely valuable. The fit of two-pion photoproduction data suggests a substantial coupling of $P_{13}(1720)$ to the $D_{13}(1520)\pi$ channel. Thus we observe here a double pole structure near the $D_{13}(1520)\pi$ threshold which results in rather large errors and in difficulties to identify the corresponding Breit-Wigner parameters. We believe that the forthcoming polarization data on two-pion photoproduction will improve significantly the accuracy in the definition of $P_{13}(1720)$ pole structure. A more precise definition of the $P_{13}(1720)$ pole with its $N\pi\pi$ couplings

Table 7. Pole position (in MeV), photo-couplings calculated as residues in the pole (in $\text{GeV}^{-1/2} 10^3$, phases in degrees) and corresponding Breit-Wigner parameters for states contributing strongly to pion photoproduction (the branching ratios are in percents). The PDG values are given in parentheses. For $F_{35}(1905)$ two solutions are given.

State	$S_{11}(1535)$	$S_{11}(1650)$
Re(pole)	1510 ± 25 (1510 ± 20)	1670 ± 35 (1655 ± 15)
-2Im(pole)	140 ± 30 (170 ± 80)	170 ± 40 (165 ± 15)
$A^{1/2}(\gamma p)$	90 ± 25 / $0^\circ \pm 45^\circ$	65 ± 30 / $28^\circ \pm 15^\circ$
M_{BW}	1535 ± 20 (1535 ± 10)	1680 ± 40 (1658 ± 12)
Γ_{BW}	170 ± 35 (150 ± 25)	170 ± 45 (165 ± 20)
$\Gamma_{\pi N}/\Gamma$	35 ± 15 (45 ± 10)	50 ± 25 (78 ± 18)
State	$P_{11}(1440)$	$S_{31}(1620)$
Re(pole)	1370 ± 4 (1365 ± 15)	1596 ± 7 (1600 ± 10)
-2Im(pole)	193 ± 7 (190 ± 30)	130 ± 10 (118 ± 3)
$A^{1/2}(\gamma p)$	-48 ± 12 / $-58^\circ \pm 20^\circ$	62 ± 10 / $-0^\circ \pm 20^\circ$
M_{BW}	1440 ± 12 (1445 ± 25)	1625 ± 10 (1630 ± 30)
Γ_{BW}	335 ± 50 (325 ± 125)	148 ± 15 (143 ± 8)
$\Gamma_{\pi N}/\Gamma$	60 ± 6 (65 ± 15)	23 ± 5 (25 ± 5)
State	$P_{11}(1710)$	$P_{33}(1232)$
Re(pole)	1708 ± 18 (1720 ± 50)	1211 ± 1 (1210 ± 1)
-2Im(pole)	200 ± 20 (230 ± 150)	100 ± 2 (100 ± 2)
$A^{1/2}(\gamma p)$	24 ± 8 / $-20^\circ \pm 60^\circ$	-136 ± 5 / $-17^\circ \pm 5^\circ$
$A^{3/2}(\gamma p)$		-267 ± 8 / $-3^\circ \pm 3^\circ$
M_{BW}	1725 ± 25 (1710 ± 30)	1230 ± 2 (1232 ± 1)
Γ_{BW}	200 ± 35 (150 ± 100)	112 ± 4 (118 ± 2)
$\Gamma_{\pi N}/\Gamma$	12 ± 6 (15 ± 5)	100 (100)
State	$P_{13}(1720)$	$D_{33}(1700)$
Re(pole)	1660 ± 35 (1675 ± 15)	1650 ± 30 (1650 ± 30)
-2Im(pole)	360 ± 80 (190 ± 85)	275 ± 35 (200 ± 40)
$A^{1/2}(\gamma p)$	140 ± 50 / $-35^\circ \pm 25^\circ$	160 ± 45 / $35^\circ \pm 12^\circ$
$A^{3/2}(\gamma p)$	110 ± 50 / $10^\circ \pm 35^\circ$	165 ± 40 / $40^\circ \pm 18^\circ$
M_{BW}	1770 ± 100 (1725 ± 25)	1780 ± 40 (1710 ± 40)
Γ_{BW}	650 ± 120 (225 ± 75)	580 ± 120 (300 ± 100)
$\Gamma_{\pi N}/\Gamma$	14 ± 5 (15 ± 5)	16 ± 7 (15 ± 5)
State	$D_{13}(1520)$	$F_{35}(1905)$ (sol.1)
Re(pole)	1512 ± 3 (1510 ± 5)	1800 ± 15 (1830 ± 5)
-2Im(pole)	110 ± 6 (112 ± 7)	300 ± 20 (282 ± 18)
$A^{1/2}(\gamma p)$	-30 ± 6 / $15^\circ \pm 10^\circ$	28 ± 10 / $-35^\circ \pm 15^\circ$
$A^{3/2}(\gamma p)$	130 ± 6 / $6^\circ \pm 5^\circ$	-42 ± 12 / $-25^\circ \pm 15^\circ$
M_{BW}	1524 ± 4 (1520 ± 5)	1890 ± 25 (1890 ± 25)
Γ_{BW}	117 ± 6 (112 ± 13)	335 ± 30 (335 ± 65)
$\Gamma_{\pi N}/\Gamma$	57 ± 5 (60 ± 5)	12 ± 3 (12 ± 3)
State	$D_{15}(1675)$	$F_{35}(1905)$ (sol.2)
Re(pole)	1650 ± 5 (1660 ± 5)	1805 ± 15 (1830 ± 5)
-2Im(pole)	143 ± 7 (138 ± 12)	310 ± 20 (282 ± 18)
$A^{1/2}(\gamma p)$	20 ± 4 / $-6^\circ \pm 6^\circ$	47 ± 10 / $-30^\circ \pm 12^\circ$
$A^{3/2}(\gamma p)$	24 ± 8 / $-6^\circ \pm 6^\circ$	0 ± 3
M_{BW}	1678 ± 5 (1675 ± 5)	1850 ± 20 (1890 ± 25)
Γ_{BW}	177 ± 15 (148 ± 18)	345 ± 30 (335 ± 65)
$\Gamma_{\pi N}/\Gamma$	37 ± 5 (40 ± 5)	12 ± 3 (12 ± 3)
State	$F_{15}(1680)$	$F_{37}(1950)$
Re(pole)	1672 ± 4 (1673 ± 8)	1882 ± 8 (1880 ± 10)
-2Im(pole)	114 ± 12 (133 ± 12)	262 ± 12 (240 ± 20)
$A^{1/2}(\gamma p)$	-12 ± 6 / $-45^\circ \pm 30^\circ$	-81 ± 8 / $-15^\circ \pm 12^\circ$
$A^{3/2}(\gamma p)$	130 ± 8 / $0^\circ \pm 10^\circ$	-93 ± 8 / $-15^\circ \pm 15^\circ$
M_{BW}	1685 ± 5 (1685 ± 5)	1928 ± 8 (1933 ± 18)
Γ_{BW}	117 ± 12 (130 ± 10)	290 ± 14 (285 ± 50)
$\Gamma_{\pi N}/\Gamma$	66 ± 8 (68 ± 3)	44 ± 8 (40 ± 5)

Table 8. Helicity amplitudes $A_{1/2}$ and $A_{3/2}$ for N^* and Δ^* from this work, from SAID08 [21], from MAID07 [22], from the Gießen model [23, 24] and estimates from Ref. [1].

Resonance	$A_{1/2}$ ($\text{GeV}^{-1/2} \times 10^3$)					$A_{3/2}$ ($\text{GeV}^{-1/2} \times 10^3$)				
	BnGa09	FA08	MAID07	Gießen	PDG	BnGa09	FA08	MAID07	Gießen	PDG
$S_{11}(1535)$	90 ± 15	100.9 ± 3.0	66	95	90 ± 30					
$S_{11}(1650)$	60 ± 20	9.0 ± 9.1	33	57	53 ± 16					
$P_{11}(1440)$	-52 ± 10	-56.4 ± 1.7	-61	-84	-65 ± 4					
$P_{11}(1710)$	25 ± 10			-50	9 ± 22					
$P_{13}(1720)$	130 ± 50	90.5 ± 3.3	73	-65	18 ± 30	100 ± 50	-36.0 ± 3.9	-11	35	-19 ± 20
$D_{13}(1520)$	-32 ± 6	-26 ± 1.5	-27	-15	-24 ± 9	138 ± 8	141.2 ± 1.7	161	146	166 ± 5
$D_{15}(1675)$	21 ± 4	14.9 ± 2.1	15	9	19 ± 8	24 ± 8	18.4 ± 2.1	22	21	15 ± 9
$F_{15}(1680)$	-12 ± 6	-17.6 ± 1.5	-25	3	-15 ± 6	136 ± 12	134.2 ± 1.6	134	116	133 ± 12
$S_{31}(1620)$	63 ± 12	47.2 ± 2.3	66	-50	27 ± 11					
$P_{33}(1232)$	-136 ± 5	-139.6 ± 1.8	-140	-128	-135 ± 6	-267 ± 8	-258.9 ± 2.3	-265	-247	-250 ± 8
$D_{33}(1700)$	160 ± 45	118.3 ± 3.3	226	96	104 ± 15	160 ± 40	110.0 ± 3.5	210	154	85 ± 22
$F_{35}(1905)$	28 ± 12	11.4 ± 8.0	18		26 ± 11	-42 ± 15	-51.0 ± 8.0	-28		-45 ± 20
or:	(48 ± 12)					(0 ± 3)				
$F_{37}(1950)$	-83 ± 8	-71.5 ± 1.8	-94		-76 ± 12	-92 ± 8	-96 ± 8	-121		-97 ± 10

may also help to resolve the discrepancies in the determination of its $A_{3/2}$ helicity amplitude when different analyses are compared.

The Review of Particle Properties lists Breit-Wigner parameters and real helicity amplitudes. In the K-matrix approach, a photo-produced resonance is described by a P-vector (eq. 12). Even if the photo-coupling constant $g_{\gamma N}^{(\alpha)}$ is real, the photo-coupling at the resonance position, calculated as residuum of the amplitude P_b at the pole, will in general be complex. To allow for a comparison with other determinations, we define helicity amplitudes by the following procedure: a Breit-Wigner amplitude is constructed with an adjustable mass and a width which is parameterized as a sum of all partial widths, $\sum \rho_i g_i^2$. The total widths is scaled with one parameter. This scaling parameter as well as the Breit-Wigner mass are adjusted to reproduce the pole position of the P-vector amplitude. The Breit-Wigner helicity amplitudes $A_{1/2}$ and $A_{3/2}$ are defined by the condition that the residues of the Breit-Wigner photoproduction amplitude reproduce the magnitude of the original residues of the P-vector/K-matrix amplitude.

In Table 8 we compare our results on $A_{1/2}$ and $A_{3/2}$ for N^* and Δ^* with previous determinations of these quantities. These real helicity amplitudes are given in Table 8 and compared to values obtained by SAID, MAID, and the Gießen model, and to the values listed by the PDG [1]. First we notice that our errors are much larger than those given by FA08, MAID and Gießen do not give any errors. We believe that the FA08 systematic errors are underestimated: the impact of variations in the couplings to inelastic channels can hardly be tested using only reactions with $N\pi$ in the final state. The errors we quote are not statistical errors; those are small. Our errors are

derived from a large number of fits changing the number of resonances, switching on and off couplings to inelastic channels, using different start values for the fits.

For most resonances, reasonable consistency between the different analyses is found. In particular the helicity amplitudes for photoproduction of the Roper resonance from SAID, MAID, and BnGa are fully consistent (the Gießen result is a bit higher) even though mass, width, and $N\pi$ decay branching fractions differ somewhat. BnGa and SAID, e.g., find, respectively,

	M (MeV)	Γ (MeV)	$\Gamma_{N\pi}/\Gamma_{\text{tot}}$
BnGa	1440 ± 12	335 ± 50	0.60 ± 0.06
FA08	1485	284	0.79

In our analysis, the Roper resonance is fully constrained: from three of the four reactions, πN elastic scattering, $\gamma p \rightarrow N\pi$, $\pi^- p \rightarrow p\pi^0\pi^0$, and $\gamma p \rightarrow p\pi^0\pi^0$, the amplitude for the forth reaction can be predicted. Hence we are particularly confident that these results are correct.

We comment briefly on further differences. The PDG result for the $A_{1/2}$ amplitude of $(53 \pm 16) \text{ GeV}^{-1/2} \times 10^3$ for producing $S_{11}(1650)$ was driven by the 1995 VPI result $(69 \pm 5) \text{ GeV}^{-1/2} \times 10^3$ [155] and by the small value $(22 \pm 7) \text{ GeV}^{-1/2} \times 10^3$ obtained in [47]. The most recent FA08 analysis gives $(9.0 \pm 9.1) \text{ GeV}^{-1/2} \times 10^3$, a value which is much smaller and which is not confirmed here; we find $(60 \pm 20) \text{ GeV}^{-1/2} \times 10^3$, in close agreement with the Gießen result. Part of the discrepancy with FA08 is certainly due to the $S_{11}(1650)$ branching ratio to the πN channel; in FA08 this is fixed to be 100% while we find $(50 \pm 25)\%$. Of course, photoproduction defines only the product of the helicity and πN couplings.

Possibly related are the differences in the helicity amplitudes for $P_{13}(1720)$. Our value for $A_{1/2}$ is compatible with the new FA08 analysis and in conflict with the

value quoted by the PDG. Incompatible with all other determinations - even in the sign - is our value for the $A_{3/2}$ helicity amplitude for $P_{13}(1720)$ production. Also the Gießen results are at variance with the other determinations. Clearly, more data are required to resolve this discrepancy; the results from double polarization experiments carried out at present in different laboratories will very likely be decisive.

There is the possibility, that the discrepancies in the properties of $P_{13}(1720)$ have a physical origin. In [156] it was found that data on the reaction $ep \rightarrow e'p\pi^+\pi^-$ could be described only when resonance parameters were drastically changed with respect to published results, or when a new resonance in the P_{13} wave was introduced. Apparently, the $P_{13}(1720)$ properties are different in $N\pi$ and in $N\pi\pi$; this might be a hint for the presence of a close-by state in the same partial wave.

5 Summary

We have presented results from a partial wave analysis on a large variety of different reactions, from πN elastic scattering to photoproduction of multibody final states. The main emphasis of this paper was devoted to a determination of the electric and magnetic multipoles leading to the production of neutral or charged pions in photo-induced reactions off protons. The multipoles are mostly consistent with previous analyses but a few significant discrepancies call for clarifications. The analysis provides masses, widths, and helicity amplitudes for several known resonances. Masses and widths and the πN partial decay widths of all resonances agree very well with established values. Only the photocoupling of the $P_{13}(1720)$ resonance differs remarkably from PDG and from the values found in a recent analysis of the CLAS collaboration. This discrepancy may be a further hint for the conjecture [156] that the $P_{13}(1720)$ resonance may have a more complicated structure than usually assumed.

Acknowledgements

We would like to thank the members of SFB/TR16 for continuous encouragement. We acknowledge financial support from the Deutsche Forschungsgemeinschaft (DFG) within the SFB/TR16 and from the Forschungszentrum Jülich within the FFE program. The collaboration with St. Petersburg received funds from DFG and the Russian Foundation for Basic Research.

Appendix A: The structure of the fermion propagator

We consider scattering of two particles with momenta k_1 and k_2 in the initial and q_1 and q_2 in the final state. There are three independent momenta. It is convenient to choose the total four-momentum of the system $P = k_1 + k_2 =$

$q_1 + q_2$ and two relative momenta k_μ^\perp and q_μ^\perp which are orthogonal to the total momentum:

$$k_\mu^\perp = \frac{1}{2}(k_1 - k_2)_\nu g_{\mu\nu}^\perp, \quad q_\mu^\perp = \frac{1}{2}(q_1 - q_2)_\nu g_{\mu\nu}^\perp, \\ g_{\mu\nu}^\perp = \left(g_{\mu\nu} - \frac{P_\mu P_\nu}{P^2} \right). \quad (19)$$

The tensor $F_{\nu_1 \dots \nu_n}^{\mu_1 \dots \mu_n}$ depends only on the total momentum P ($s = P^2$) and describes the tensor structure of the partial wave. It can be calculated as a product of two polarization tensors $\Psi_{\nu_1 \dots \nu_n}^\alpha$ summed over possible polarizations:

$$F_{\nu_1 \dots \nu_n}^{\mu_1 \dots \mu_n} = \sum_\alpha \Psi_{\mu_1 \dots \mu_n}^{\alpha*} \Psi_{\nu_1 \dots \nu_n}^\alpha. \quad (20)$$

For every set of indices, $F_{\nu_1 \dots \nu_n}^{\mu_1 \dots \mu_n}$ satisfies the properties of the polarization tensor: it is symmetrical over permutation of any two indices, traceless and for $n > 0$ is orthogonal to the total momentum of the system. It usually normalized by the condition:

$$F_{\nu_1 \dots \nu_n}^{\mu_1 \dots \mu_n} F_{\xi_1 \dots \xi_n}^{\nu_1 \dots \nu_n} = (-1)^n F_{\xi_1 \dots \xi_n}^{\mu_1 \dots \mu_n}. \quad (21)$$

and is often called projection operator: its convolution with another tensor by one set of indices results in a tensor which obeys the symmetry properties of the corresponding partial wave.

In the case of a fermionic system, $F_{\nu_1 \dots \nu_n}^{\mu_1 \dots \mu_n}$ can be written in the form

$$F_{\nu_1 \dots \nu_n}^{\mu_1 \dots \mu_n} = (-1)^n \frac{\sqrt{s} + \hat{P}}{2\sqrt{s}} O_{\xi_1 \dots \xi_n}^{\mu_1 \dots \mu_n} T_{\beta_1 \dots \beta_n}^{\xi_1 \dots \xi_n} O_{\nu_1 \dots \nu_n}^{\beta_1 \dots \beta_n}. \quad (22)$$

Here, $(\sqrt{s} + \hat{P})$ corresponds to the numerator of a propagator describing a particle with $J = 1/2$ and $n = J - 1/2$ ($\sqrt{s} = M$ for the stable particle). We define

$$T_{\beta_1 \dots \beta_n}^{\xi_1 \dots \xi_n} = \frac{n+1}{2n+1} (g_{\xi_1 \beta_1} - \frac{n}{n+1} \sigma_{\xi_1 \beta_1}) \prod_{i=2}^n g_{\xi_i \beta_i}, \quad (23)$$

$$\sigma_{\alpha_i \alpha_j} = \frac{1}{2} (\gamma_{\alpha_i} \gamma_{\alpha_j} - \gamma_{\alpha_j} \gamma_{\alpha_i}). \quad (24)$$

We introduced the factor $1/(2\sqrt{s})$ in the propagator which removes the divergency of this function at large energies. For the stable particle it means that bispinors are normalized as follows:

$$\bar{u}(k_N) u(k_N) = 1, \quad \sum_{polarizations} u(k_N) \bar{u}(k_N) = \frac{m + \hat{k}_N}{2m}. \quad (25)$$

Here and below, $\hat{k} \equiv \gamma_\mu k_\mu$.

The boson projection operator $O_{\nu_1 \dots \nu_n}^{\mu_1 \dots \mu_n}$ has the following properties:

$$P_{\mu_i} O_{\nu_1 \dots \nu_n}^{\mu_1 \dots \mu_n} = P_{\nu_j} O_{\nu_1 \dots \nu_n}^{\mu_1 \dots \mu_n} = 0, \\ g_{\mu_i \mu_j} O_{\nu_1 \dots \nu_n}^{\mu_1 \dots \mu_n} = g_{\nu_i \nu_j} O_{\nu_1 \dots \nu_n}^{\mu_1 \dots \mu_n} = 0, \\ O_{\alpha_1 \dots \alpha_n}^{\mu_1 \dots \mu_n} O_{\nu_1 \dots \nu_n}^{\alpha_1 \dots \alpha_n} = (-1)^n O_{\nu_1 \dots \nu_n}^{\mu_1 \dots \mu_n}. \quad (26)$$

For the lowest states,

$$O = 1, \quad O_\nu^\mu = g_{\mu\nu}^\perp, \\ O_{\nu_1\nu_2}^{\mu_1\mu_2} = \frac{1}{2} \left(g_{\mu_1\nu_1}^\perp g_{\mu_2\nu_2}^\perp + g_{\mu_1\nu_2}^\perp g_{\mu_2\nu_1}^\perp - \frac{2}{3} g_{\mu_1\mu_2}^\perp g_{\nu_1\nu_2}^\perp \right). \quad (27)$$

For higher states, the operator can be calculated using the recurrent expression:

$$O_{\nu_1\dots\nu_n}^{\mu_1\dots\mu_n} = \frac{1}{n^2} \left(\sum_{i,j=1}^n g_{\mu_i\nu_j}^\perp O_{\nu_1\dots\nu_{j-1}\nu_{j+1}\dots\nu_n}^{\mu_1\dots\mu_{i-1}\mu_{i+1}\dots\mu_n} \right. \\ \left. - \frac{4}{(2n-1)(2n-3)} \times \sum_{\substack{i < j \\ k < m}}^n g_{\mu_i\nu_j}^\perp g_{\mu_k\nu_m}^\perp O_{\nu_1\dots\nu_{k-1}\nu_{k+1}\dots\nu_{m-1}\nu_{m+1}\dots\nu_n}^{\mu_1\dots\mu_{i-1}\mu_{i+1}\dots\mu_{j-1}\mu_{j+1}\dots\mu_n} \right). \quad (28)$$

The tensor $F_{\nu_1\dots\nu_n}^{\mu_1\dots\mu_n}$ has all orthogonality properties of the tensor $O_{\nu_1\dots\nu_n}^{\mu_1\dots\mu_n}$ plus orthogonality to the γ -matrix:

$$\gamma_{\mu_i} F_{\nu_1\dots\nu_n}^{\mu_1\dots\mu_n} = F_{\nu_1\dots\nu_n}^{\mu_1\dots\mu_n} \gamma_{\nu_j} = 0. \quad (29)$$

The pseudoscalar meson-nucleon vertices for the partial wave with spin J have the form:

$$Q_{\mu_1\dots\mu_n}^{(+)} = X_{\mu_1\dots\mu_n}^{(n)}(q^\perp) u(q_1), \\ Q_{\mu_1\dots\mu_n}^{(-)} = i\gamma_5 \gamma_\nu X_{\nu\mu_1\dots\mu_n}^{(n+1)}(q^\perp) u(q_1), \quad (30)$$

where $n = J - 1/2$ and $u(q_1)$ is the bispinor of the baryon. The '+' and '-' indices describe two sets of the partial waves with relation between orbital momentum L and the total spin J as $J = L + 1/2$ ('+' partial waves) and $J = L - 1/2$ ('-' partial waves). The '+' set of vertices describes the partial waves with $J^P = \frac{1}{2}^-, \frac{3}{2}^+, \frac{5}{2}^- \dots$ and the second set $J^P = \frac{1}{2}^+, \frac{3}{2}^-, \frac{5}{2}^+ \dots$

In the case of virtual photons there are, for every partial wave with $J > 1/2$, three γ^*N vertices; for real photons, only two of them are independent [151]. In the LS formalism these vertices correspond to spin 1/2 and 3/2 of the photon-nucleon system. For '+' states the vertices are (following the ordering in [151]):

$$Q_{\alpha_1\dots\alpha_n}^{(1+)} = \bar{u}(k_1) \gamma_\mu^\perp i\gamma_5 X_{\alpha_1\dots\alpha_n}^{(n)}(k^\perp) \varepsilon_\mu, \\ Q_{\alpha_1\dots\alpha_n}^{(3+)} = \bar{u}(k_1) \gamma_\nu i\gamma_5 X_{\nu\alpha_1\dots\alpha_{n-1}}^{(n)}(k^\perp) g_{\mu\alpha_n}^\perp \varepsilon_\mu, \quad (31)$$

where $\bar{u}(k_1)$ is bispinor of the initial nucleon and ε_μ is the photon polarization vector.

For '-' states we have:

$$Q_{\alpha_1\dots\alpha_n}^{(1-)} = \bar{u}(k_1) \gamma_\xi^\perp \gamma_\mu^\perp \varepsilon_\mu X_{\xi\alpha_1\dots\alpha_n}^{(n+1)}(k^\perp), \\ Q_{\alpha_1\dots\alpha_n}^{(3-)} = \bar{u}(k_1) X_{\alpha_2\dots\alpha_n}^{(n-1)}(k^\perp) g_{\alpha_1\mu}^\perp \varepsilon_\mu. \quad (32)$$

The orbital angular momentum operators for $L \leq 3$ are:

$$X^{(0)} = 1, \quad X_\mu^{(1)} = k_\mu^\perp,$$

Fig. 14. Diagram representation of eq. (2)

$$X_{\mu_1\mu_2}^{(2)} = \frac{3}{2} \left(k_{\mu_1}^\perp k_{\mu_2}^\perp - \frac{1}{3} k_\perp^2 g_{\mu_1\mu_2}^\perp \right), \\ X_{\mu_1\mu_2\mu_3}^{(3)} = \frac{5}{2} \left[k_{\mu_1}^\perp k_{\mu_2}^\perp k_{\mu_3}^\perp - \frac{k_\perp^2}{5} (g_{\mu_1\mu_2}^\perp k_{\mu_3}^\perp + g_{\mu_1\mu_3}^\perp k_{\mu_2}^\perp + g_{\mu_2\mu_3}^\perp k_{\mu_1}^\perp) \right]. \quad (33)$$

The operator $X_{\nu\mu_1\dots\mu_n}^{(n+1)}$ can be written as a series of products of metric tensors and relative momentum vectors. The first term is proportional to the production of relative momentum vectors k_μ^\perp , other terms correspond to the substitution of two vectors by a metric tensor with corresponding indices:

$$X_{\nu\mu_1\dots\mu_n}^{(n+1)}(k^\perp) = \alpha_{n+1} \left[k_\nu^\perp k_{\mu_1}^\perp k_{\mu_2}^\perp k_{\mu_3}^\perp \dots k_{\mu_n}^\perp - \frac{k_\perp^2}{2n+1} \right. \\ \times \left(\sum_{i=1}^n g_{\nu\mu_i}^\perp \prod_{j \neq i} k_{\mu_j}^\perp + \sum_{i < j}^n g_{\mu_i\mu_j}^\perp k_\nu^\perp \prod_{m \neq i \neq j} k_{\mu_m}^\perp + \dots \right) \\ \left. + \frac{k_\perp^4}{(2n+1)(2n-1)} \left(\sum_{i,j < m}^n g_{\nu\mu_i}^\perp g_{\mu_j\mu_m}^\perp \prod_{l \neq i \neq j \neq m} k_{\mu_l}^\perp \right. \right. \\ \left. \left. + \sum_{i < k, j < m}^n g_{\mu_i\mu_k}^\perp g_{\mu_j\mu_m}^\perp k_\nu^\perp \prod_{\substack{l \neq i \neq k \\ \neq j \neq m}} k_{\mu_l}^\perp + \dots \right) + \dots \right]. \quad (34)$$

Appendix B: Contribution of the loop diagrams

For the πN vertices we have [151]:

$$W_n^{(+)} = (-1)^n \frac{\alpha_n}{2n+1} |\mathbf{k}|^{2n} \frac{m_N + k_{10}}{2m_N}, \\ W_n^{(-)} = (-1)^n \frac{\alpha_{n+1}}{n+1} |\mathbf{k}|^{2n+2} \frac{m_N + k_{10}}{2m_N}, \quad (35)$$

and for the γN vertices (in the case of photoproduction):

$$W_n^{(11+)} = (-1)^n 2 \frac{\alpha_n}{2n+1} |\mathbf{k}|^{2n} \frac{m_N + k_{10}}{2m_N}, \\ W_n^{(33+)} = (-1)^n \frac{\alpha_n}{2n+1} \frac{(n+1)}{n} |\mathbf{k}|^{2n} \frac{m_N + k_{10}}{2m_N}, \\ W_n^{(13+)} = (-1)^n \frac{\alpha_n}{2n+1} |\mathbf{k}|^{2n} \frac{m_N + k_{10}}{2m_N}. \quad (36)$$

for the '+' states and

$$W_n^{(11-)} = (-1)^n \frac{2\alpha_{n+1}}{n+1} |\mathbf{k}|^{2n+2} \frac{m_N + k_{10}}{2m_N},$$

$$W_n^{(33-)} = (-1)^n \frac{\alpha_{n-1}(n+1)}{(2n+1)(2n-1)} |\mathbf{k}|^{2n-2} \frac{m_N + k_{10}}{2m_N},$$

$$W_n^{(13-)} = (-1)^n \frac{\alpha_{n-1}}{n+1} |\mathbf{k}|^{2n} \frac{m_N + k_{10}}{2m_N} \quad (37)$$

for the '-' states. The γN vertices in this representation are not orthogonal to each other, and to extract partial waves one needs to solve a 2×2 system of linear equations.

Appendix C: Single meson photoproduction amplitude

The general structure of the single-meson photoproduction amplitude in c.m.s. of the reaction is given by

$$J_\mu = i\mathcal{F}_1 \sigma_\mu + \mathcal{F}_2(\sigma \mathbf{q}) \frac{\varepsilon_{\mu ij} \sigma_i k_j}{|\mathbf{k}||\mathbf{q}|} + i\mathcal{F}_3 \frac{(\sigma \mathbf{k})}{|\mathbf{k}||\mathbf{q}|} q_\mu + i\mathcal{F}_4 \frac{(\sigma \mathbf{q})}{\mathbf{q}^2} q_\mu,$$

$$A = \omega^* J_\mu \varepsilon_\mu \omega', \quad (38)$$

where \mathbf{q} is the momentum of the nucleon in the πN channel and \mathbf{k} the momentum of the nucleon in the γN channel calculated in the c.m.s. of the reaction. The σ_i are Pauli matrices and ω, ω' are non relativistic spinors of initial and final states correspondingly.

If \mathcal{F}_i are known, e.g. from the t or u channel exchange amplitudes calculated in the c.m.s. of the reaction, the partial wave amplitudes can be obtained as

$$A_n^{(i\pm)} = \int_{-1}^1 \frac{dz}{2} \mathcal{F}_m D_m^{(i\pm)}, \quad (39)$$

where z is the cosine of the angle between initial and final relative momenta and vectors $D^{(i\pm)}$ are equal to

$$D^{(1+)} = \frac{1}{\kappa_n \alpha_n} \left(P_n, -P_{n+1}, 0, \frac{(1-z^2)P'_{n+1}}{(n+1)(n+2)} \right),$$

$$D^{(2+)} = \frac{1-z^2}{\kappa_n \alpha_n} \left(0, 0, \frac{P'_n}{(n+1)}, \frac{nP'_{n+1}}{(n+1)(n+2)} \right),$$

$$D^{(1-)} = -\frac{n+1}{\kappa_{n+1} \alpha_{n+1}} \left(-P_{n+1}, P_n, \frac{(1-z^2)P'_{n+1}}{(n+1)(n+2)}, 0 \right),$$

$$D^{(2-)} = -\frac{1-z^2}{\kappa_{n-1} \alpha_{n-1} |\mathbf{k}|^2} \left(0, 0, \frac{nP'_{n+1}}{(n+2)}, P'_n \right). \quad (40)$$

Here $P_n = P_n(z)$ are Legendre polynomials and $P'_n = dP_n(z)/dz$.

Using the multipole decomposition of the $A_n^{(i\pm)}$ amplitudes given in [150] one can obtain the standard expression for the projection of the total amplitude into multipoles.

Appendix D: Reggeon propagator parametrization

In this section we give the expressions for Reggeon propagators used in the fit.

The propagator for pion exchange has the form

$$R_\pi(+, \nu, t) = \frac{e^{-i\frac{\pi}{2}\alpha_\pi(t)}}{\sin(\frac{\pi}{2}\alpha_\pi(t))\Gamma\left(\frac{\alpha_\pi(t)}{2} + 1\right)} \left(\frac{\nu}{\nu_0}\right)^{\alpha_\pi(t)}, \quad (41)$$

where $\alpha_\pi(t) = -0.014 + 0.72t$ is a function defining the trajectory, ν_0 is a normalization factor (which can be taken to be 1). The Γ -function is introduced in the denominator to eliminate the additional poles at $t < 0$. The propagator for Kaon exchange is given by

$$R_K(+, \nu, t) = \frac{e^{-i\frac{\pi}{2}\alpha_K(t)}}{\sin(\frac{\pi}{2}\alpha_K(t))\Gamma\left(\frac{\alpha_K(t)}{2} + 1\right)} \left(\frac{\nu}{\nu_0}\right)^{\alpha_K(t)}, \quad (42)$$

where $\alpha_K(t) = -0.25 + 0.85t$.

The propagator for K^* exchange is identical to the ρ exchange propagator but has $\alpha_{K^*}(t) = 0.32 + 0.85t$.

References

1. C. Amsler *et al.*, Phys. Lett. B **667**, 1 (2008).
2. S. Capstick and N. Isgur, Phys. Rev. D **34** (1986) 2809.
3. L. Y. Glozman *et al.*, Phys. Rev. D **58** (1998) 094030.
4. U. Löring *et al.*, Eur. Phys. J. A **10** (2001) 395, 447.
5. S. Capstick and W. Roberts, Phys. Rev. D **47**, 1994 (1993).
6. R. A. Arndt *et al.*, Phys. Rev. C **74**, 045205 (2006).
7. M. Anselmino *et al.*, Rev. Mod. Phys. **65** (1993) 1199.
8. M. Kirchbach, M. Moshinsky and Yu. F. Smirnov, Phys. Rev. D **64** (2001) 114005.
9. R. L. Jaffe and F. Wilczek, Phys. Rev. Lett. **91** (2003) 232003.
10. R. L. Jaffe, Phys. Rept. **409** (2005) 1 [Nucl. Phys. Proc. Suppl. **142** (2005) 343].
11. N. Kaiser, P. B. Siegel and W. Weise, Nucl. Phys. A **594**, 325 (1995).
12. L. Y. Glozman, Phys. Lett. B **587**, 69 (2004).
13. L. Y. Glozman, Phys. Rept. **444**, 1 (2007).
14. G. F. de Teramond and S. J. Brodsky, Phys. Rev. Lett. **94**, 201601 (2005).
15. S. J. Brodsky and G. F. de Teramond, Phys. Rev. D **77**, 056007 (2008).
16. H. Forkel, M. Beyer and T. Frederico, JHEP **0707**, 077 (2007).
17. H. Forkel and E. Klempt, Phys. Lett. B **679**, 77 (2009).
18. A. J. G. Hey and R. L. Kelly, Phys. Rept. **96**, 71 (1983).
19. S. Capstick and W. Roberts, Prog. Part. Nucl. Phys. **45**, S241 (2000).
20. E. Klempt and J. M. Richard, "Baryon spectroscopy," (Review of Modern Physics) arXiv:0901.2055 [hep-ph].
21. WWW.GWDAC.PHYS.GWU.EDU/
22. WWW.KPH.UNI-MAINZ.DE/MAID/
23. G. Penner and U. Mosel, Phys. Rev. C **66**, 055212 (2002).
24. V. Shklyar, H. Lenske and U. Mosel, Phys. Lett. B **650**, 172 (2007).
25. W. Deinet *et al.*, Nucl. Phys. B **11**, 495 (1969).
26. W. B. Richards *et al.*, Phys. Rev. D **1**, 10 (1970).
27. R. M. Brown *et al.*, Nucl. Phys. B **153**, 89 (1979).
28. S. Prakhov *et al.*, Phys. Rev. C **72**, 015203 (2005).
29. N. C. Debenham *et al.*, Phys. Rev. D **12**, 2545 (1975).

30. H. R. Crouch *et al.*, Phys. Rev. D **21**, 3023 (1980).
31. J. Durand *et al.*, Phys. Rev. C **78**, 025204 (2008).
32. S. Prakhov *et al.*, Phys. Rev. C **69**, 045202 (2004).
33. U. Thoma *et al.*, Phys. Lett. B **659**, 87 (2008).
34. A. V. Sarantsev *et al.*, Phys. Lett. B **659**, 94 (2008).
35. C. Weinheimer, Nucl. Phys. A **721** (2003) 781.
36. I. Horn *et al.*, Phys. Rev. Lett. **101**, 202002 (2008).
37. I. Horn *et al.*, Eur. Phys. J. A **38**, 173 (2008).
38. Y. Assafiri *et al.*, Phys. Rev. Lett. **90**, 222001 (2003).
39. E. Gutz *et al.*, Eur. Phys. J. A **35**, 291 (2008).
40. J. Ahrens *et al.*, Eur. Phys. J. A **34** 11, (2007).
41. M. Fuchs *et al.*, Phys. Lett. B **368**, 20 (1996).
42. J. Ahrens *et al.*, Phys. Rev. Lett. **88**, 232002 (2002).
43. J. Ahrens *et al.*, Eur. Phys. J. A **21**, 323 (2004).
44. O. Bartalini *et al.*, Eur. Phys. J. A **26**, 399 (2005).
45. O. Bartholomy *et al.*, Phys. Rev. Lett. **94**, 012003 (2005).
46. H. van Pee *et al.*, Eur. Phys. J. A **31**, 61 (2007).
47. M. Dugger *et al.*, Phys. Rev. C **76**, 025211 (2007).
48. G. Barbiellini *et al.*, Phys. Rev. **184**, 1402 (1969).
49. V. G. Gorbenko *et al.*, Pisma Zh. Eksp. Teor. Fiz. **19**, 659 (1974).
50. V. G. Gorbenko *et al.*, Yad. Fiz. **27**, 1204 (1978).
51. A. a. Belyaev *et al.*, Nucl. Phys. B **213**, 201 (1983).
52. G. Blanpied *et al.*, Phys. Rev. Lett. **69**, 1880 (1992).
53. R. Beck *et al.*, Phys. Rev. Lett. **78**, 606 (1997).
54. F. V. Adamian *et al.*, Phys. Rev. C **63**, 054606 (2001).
55. G. Blanpied *et al.*, Phys. Rev. C **64**, 025203 (2001).
56. P. S. L. Booth *et al.*, Nucl. Phys. B **121**, 45 (1977).
57. P. Feller *et al.*, Nucl. Phys. B **110**, 397 (1976).
58. V. G. Gorbenko *et al.*, Yad. Fiz. **26**, 320 (1977).
59. H. Herr *et al.*, Nucl. Phys. B **125**, 157 (1977).
60. M. Fukushima *et al.*, Nucl. Phys. B **136**, 189 (1978).
61. P. J. Bussey *et al.*, Nucl. Phys. B **154**, 492 (1979).
62. K. S. Agababian *et al.*, Sov. J. Nucl. Phys. **50**, 834 (1989) [Yad. Fiz. **50**, 1341 (1989)].
63. M. M. Asaturian *et al.*, JETP Lett. **44**, 341 (1986) [Pisma Zh. Eksp. Teor. Fiz. **44**, 266 (1986)].
64. A. Bock *et al.*, Phys. Rev. Lett. **81**, 534 (1998).
65. J. O. Maloy, Ph.D. Thesis, 1961.
66. V. G. Gorbenko *et al.*, Pisma Zh. Eksp. Teor. Fiz. **22**, 393 (1975).
67. S. Kato *et al.*, Nucl. Phys. B **168**, 1 (1980).
68. A. S. Bratashvsky *et al.*, Nucl. Phys. B **166**, 525 (1980).
69. A. S. Bratashvsky *et al.*, Ukr. Fiz. Zh. (Russ. Ed.) **31**, 1306 (1986).
70. P. J. Bussey *et al.*, Nucl. Phys. B **159**, 383 (1979).
71. J. Ahrens *et al.*, Eur. Phys. J. A **26**, 135 (2005).
72. R. O. Avakyan *et al.*, Sov. J. Nucl. Phys. **53**, 448 (1991) [Yad. Fiz. **53**, 717 (1991)].
73. S. D. Ecklund and R. L. Walker, Phys. Rev. **159**, 1195 (1967).
74. C. Betourne, J. C. Bizot, J. P. Perez-y-Jorba, D. Treille and W. Schmidt, Phys. Rev. **172**, 1343 (1968).
75. B. Bouquet *et al.*, Phys. Rev. Lett. **27**, 1244 (1971).
76. T. Fujii *et al.*, Phys. Rev. Lett. **26**, 1672 (1971).
77. K. Ekstrand *et al.*, Phys. Rev. D **6**, 1 (1972).
78. T. Fujii *et al.*, Nucl. Phys. B **120**, 395 (1977).
79. I. Arai *et al.*, J. Phys. Soc. Jap. **43**, 363 (1977).
80. E. J. Durwen, Ph.D. Thesis (1980); BONN-IR-80-7, Apr. 1980.
81. K. H. Althoff *et al.*, Z. Phys. C **18**, 199 (1983).
82. W. Heise, Ph.D. Thesis (1988); BONN-IR-88-06, Feb. 1988.
83. P. Zenz, Ph.D. Thesis (19880; BONN-IR-88-12, March 1988.
84. K. Buechler *et al.*, Nucl. Phys. A **570**, 580 (1994).
85. H. W. Dannhausen *et al.*, Eur. Phys. J. A **11**, 441 (2001).
86. J. Ahrens *et al.*, Phys. Rev. C **74**, 045204 (2006).
87. M. Dugger *et al.*, Phys. Rev. C **79**, 065206 (2009).
88. R. E. Taylor and R. F. Mozley, Phys. Rev. **117**, 835 (1960).
89. R. C. Smith and R. F. Mozley, Phys. Rev. **130**, 2429 (1963).
90. J. Alspector *et al.*, Phys. Rev. Lett. **28**, 1403 (1972).
91. G. Knies *et al.*, Phys. Rev. D **10**, 2778 (1974).
92. V. B. Ganenko *et al.*, Yad. Fiz. **23**, 100 (1976).
93. P. J. Bussey *et al.*, Nucl. Phys. B **154**, 205 (1979).
94. V. A. Getman *et al.*, Nucl. Phys. B **188**, 397 (1981).
95. P. Hampe, Ph.D. Thesis, 1980.
96. R. Beck *et al.*, Phys. Rev. C **61**, 035204 (2000).
97. J. Ajaka *et al.*, Phys. Lett. B **475**, 372 (2000).
98. J. Bocquet *et al.*, AIP Conf. Proc. **603**, 499 (2001).
99. K. H. Althoff *et al.*, Nucl. Phys. B **53**, 9 (1973).
100. S. Arai *et al.*, Nucl. Phys. B **48**, 397 (1972).
101. P. Feller *et al.*, Phys. Lett. **52B**, 105 (1974) [Nucl. Phys. B **102**, 207 (1976)].
102. K. H. Althoff *et al.*, Phys. Lett. B **59**, 93 (1975).
103. H. Genzel *et al.*, Nucl. Phys. B **92**, 196 (1975).
104. K. H. Althoff *et al.*, Phys. Lett. B **63**, 107 (1976).
105. K. H. Althoff *et al.*, Nucl. Phys. B **131**, 1 (1977).
106. M. Fukushima *et al.*, Nucl. Phys. B **130**, 486 (1977).
107. V. A. Getman *et al.*, Yad. Fiz. **32**, 1008 (1980).
108. K. Fujii *et al.*, Nucl. Phys. B **197**, 365 (1982).
109. H. Dutz *et al.*, Nucl. Phys. A **601**, 319 (1996).
110. K. Egawa *et al.*, Nucl. Phys. B **188**, 11 (1981).
111. P. J. Bussey *et al.*, Nucl. Phys. B **169**, 403 (1980).
112. A. A. Belyaev *et al.*, Yad. Fiz. **40**, 133 (1984).
113. A. A. Belyaev *et al.*, Yad. Fiz. **43**, 1469 (1986).
114. B. Krusche *et al.*, Phys. Rev. Lett. **74**, 3736 (1995).
115. M. Dugger *et al.*, Phys. Rev. Lett. **89**, 222002 (2002) [Erratum-ibid. **89**, 249904 (2002)].
116. V. Crede *et al.*, Phys. Rev. Lett. **94**, 012004 (2005).
117. O. Bartholomy *et al.*, Eur. Phys. J. A **33**, 133 (2007).
118. J. Ajaka *et al.*, Phys. Rev. Lett. **81**, 1797 (1998).
119. O. Bartalini *et al.*, Eur. Phys. J. A **33**, 169 (2007).
120. D. Elsner *et al.*, Eur. Phys. J. A **33**, 147 (2007).
121. M. Williams *et al.*, Phys. Rev. C **80** (2009) 045213.
122. V. Crede *et al.*, Phys. Rev. C **80**, 055202 (2009).
123. R. Bradford *et al.*, Phys. Rev. C **73**, 035202 (2006).
124. A. V. Sarantsev *et al.*, Eur. Phys. J. A **25**, 441 (2005).
125. K. H. Glander *et al.*, Eur. Phys. J. A **19**, 251 (2004).
126. R. G. T. Zegers *et al.*, Phys. Rev. Lett. **91**, 092001 (2003).
127. A. Lleres *et al.*, Eur. Phys. J. A **31**, 79 (2007).
128. J. W. C. McNabb *et al.*, Phys. Rev. C **69**, 042201 (2004).
129. A. Lleres *et al.*, Eur. Phys. J. A **39**, 149 (2009).
130. R. Bradford *et al.*, Phys. Rev. C **75**, 035205 (2007).
131. R. Lawall *et al.*, Eur. Phys. J. A **24**, 275 (2005).
132. R. Castelijns *et al.*, Eur. Phys. J. A **35**, 39 (2008).
133. A. Braghieri *et al.*, Phys. Lett. B **363**, 46. (1995).
134. F. Härter *et al.*, Phys. Lett. B **401**, 229 (1997).
135. A. Zabrodin *et al.*, Phys. Rev. C **55**, R1617 (1997).
136. A. Zabrodin *et al.*, Phys. Rev. C **60**, 055201 (1999).
137. M. Wolf *et al.*, Eur. Phys. J. A **9**, 5 (2000).
138. V. Kleber *et al.*, Eur. Phys. J. A **9**, 1 (2000).
139. W. Langgärtner *et al.*, Phys. Rev. Lett. **87**, 052001 (2001).
140. M. Ripani *et al.*, Phys. Rev. Lett. **91**, 022002 (2003).
141. J. Ahrens *et al.*, Phys. Lett. B **551**, 49 (2003).
142. M. Kotulla *et al.*, Phys. Lett. B **578**, 63 (2004).

- 143. J. Ahrens *et al.*, Phys. Lett. B **624** 173, (2005).
- 144. S. Strauch *et al.*, Phys. Rev. Lett. **95**, 162003 (2005).
- 145. J. Ajaka *et al.*, Phys. Lett. B **651**, 108 (2007).
- 146. D. Krambrich *et al.*, Phys. Rev. Lett. **103** (2009) 052002.
- 147. T. Nakabayashi *et al.*, Phys. Rev. C **74**, 035202 (2006).
- 148. J. Ajaka *et al.*, Phys. Rev. Lett. **100**, 052003 (2008).
- 149. V. L. Kashevarov, Eur. Phys. J. A **42**, 141 (2009) [arXiv:0901.3888 [hep-ex]].
- 150. A.V. Anisovich *et al.*, Eur. Phys. J. A **24**, 111 (2005).
- 151. A.V. Anisovich and A.V. Sarantsev, Eur. Phys. J. A **30** (2006) 427.
- 152. A. V. Anisovich, V. V. Anisovich, M. A. Matveev, V. A. Nikonov, J. Nyiri and A. V. Sarantsev, "Mesons and baryons: Systematization and methods of analysis," *Hackensack, USA: World Scientific (2008) 580 pages*.
- 153. A.V. Anisovich *et al.*, Eur. Phys. J. A **25** (2005) 427.
- 154. A pedagogical introduction to the K-matrix and P-vector approach can be found in: S. U. Chung, J. Brose, R. Hackmann, E. Klempt, S. Spanier and C. Strassburger, Annalen Phys. **4**, 404 (1995).
- 155. R. A. Arndt, I. I. Strakovsky and R. L. Workman, Phys. Rev. C **53**, 430 (1996).
- 156. M. Ripani *et al.*, Phys. Rev. Lett. **91**, 022002 (2003).